Professur für Hydrologie
Albert-Ludwigs-Universität Freiburg

Helmholtz Centre for Environmental Research – UFZ

Hanna Hennig

Multi-temporal and multi-sensor thermal analyses for submarine groundwater discharge detection over large spatial scales

Supervisor: Prof. Dr. Markus Weiler (University)
Co-Supervisor: Prof. Dr. Ralf Merz (UFZ)

Master thesis under the direction of Dr. Ulf Mallast (UFZ)

Halle/Saale, November 2014

ALBERT-LUDWIGS-UNIVERSITÄT FREIBURG

HELMHOLTZ CENTRE FOR ENVIRONMENTAL RESEARCH – UFZ

Preamble

This thesis includes methods which are adopted from the literature as well as own methods which are not yet published. In section 3 (Data and Methods) three methods are described from which the development of a cloud mask (section 3.2) is fully adopted from Zhu and Woodcock (2012). The second method copes with the calculation of a water mask (section 3.3) to extract water features by using an automated and objective image segmentation approach that is based on a scene dependent threshold and two water indices. The third method to detect submarine groundwater discharge using thermal analyses by Mallast et al. (2014) was applied and improved to be applicable to tide influenced coasts and to overcome the shortcoming of data gaps due to cloud contamination. The preprocessing of Landsat data (section 3.1) is the standard process for Landsat images.

Acknowledgement

It is a pleasure to thank those people who encouraged me in different ways and made this thesis possible.

First of all, I would like to thank Dr. Ulf Mallast who always encouraged me with his ideas and chaotic but meaningful sketches. He amused me with taking hilarious thermal pictures and sent me home in the evenings when I was lost in programming. Several times, he read my drafts and always made serious and critical suggestions.

I am grateful to Prof. Dr. Ralf Merz and Prof. Dr. Markus Weiler who agreed to supervise me.

I would like to thank all colleagues and officemates I had in this time who all showed interest on my work, made suggestions or had short and sometimes long coffee breaks with me. Special thanks to Marcel Horovitz, who I shared the office with in the first months and then travelled to Croatia where he spotted submarine springs. The pictures he took gave me the idea that the springs I was searching for do have a different shape than red pixels.

My flatmates, Marie and Jan, welcomed me home with bright and pleasing faces even late in the evening when we only had the chance to talk with brushes between teeth.

Jördis and Thomas who amused me once a week with their happy nature and supported me with cheerful board gaming evenings and events.

I would like to express my warmest gratitude to my parents for their continuous financial and mental support during all the years. Who gave me their thoughts from a different point of view, gave me the change to develop and gently threw me out of the house but always welcomed me with open arms. They spoiled me with delicious menus even when they sometimes tried to save the world. They re-illustrated my drawings and discussed them over a glass of wine. I appreciate that they gave me the opportunity to spend a year abroad.

Ehrenwörtliche Erklärung

Hiermit versichere ich, dass ich diese Abschlussarbeit selbstständig verfasst und keine anderen als die angegebenen Quellen bzw. Hilfsmittel benutzt habe und die den benutzen Werken wörtlich oder sinngemäß entnommenen Stellen als solche gekennzeichnet wurden. Zudem versichere ich, dass die Abschlussarbeit auf jeder CD mit der gedruckten Fassung in den gebundenen Exemplaren übereinstimmt.

Halle/Saale, 27. November 2014

Hanna Hennig

Abstract

The scarcity of water especially during hot and dry summer months will increase the demand on fresh water in (semi-)arid countries e.g. in the Mediterranean Sea basin (Ozyurt, 2008). Since submarine groundwater discharge (SGD) is regarded as an important component of the hydrological cycle (International Atomic Energy Agency, 2007) with an estimated global amount of groundwater seepage of 6 - 7% of the worlds rivers which is 2 400 km³ freshwater per year (Burnett et al., 2006) it is worth detecting SGD sites. In the Mediterranean it is estimated that 75% of freshwater input is contributed from karst aquifers, wherefrom a high volume is assumed to be SGD (Scientific Committee on Oceanic Research-Land-Ocean Interactions in the Coastal Zone, 2004). In this context the presented thesis aims at providing an automatised and objective approach that uses thermal satellite images from Landsat 7 and Landsat 8 to localise potential SGD sites on a large spatial scale. This objective includes the development of a water extraction algorithm to focus on the offshore areas only but likewise adapts the descriptive statistic approach from Mallast et al. (2014) to the Mediterranean Sea (MS) where three sites have been chosen to study different conditions and hence the feasibility to derive SGD sites. These adaptations include: (1) insert cloud covered scenes to enlarge the data basis, (2) implement tidal data in order to analyse low tide images as SGD is enhanced during these phases and (3) test the applicability for Landsat 8 images that will provide data in the future once Landsat 7 stops working.

In the presented thesis it could be shown that a scene based water extraction is necessary to get more accurate results. Additionally, Mediterranean SGD sites could be successfully detected using the adaptations to the method from Mallast et al. (2014).

Keywords: Landsat, large spatial scales, Mediterranean Sea, sea surface temperature, submarine groundwater discharge, water extraction

Zusammenfassung

Wasserknappheit, vor allem während der heißen und trockenen Sommermonate, wird die Nachfrage auf frisches Wasser in (semi-)ariden Ländern z. B. im Mittelmeerbecken erhöhen (Ozyurt, 2008). Da submariner Grundwasserabfluss als wichtiger Bestandteil des Wasserkreislaufes (International Atomic Energy Agency, 2007) mit einem geschätzten Gesamtbetrag von 6 - 7% des Abflusses aller Flüsse weltweit, was 2 400 km³ Süßwasser pro Jahr entspricht, gesehen wird (Burnett et al., 2006), sollte die Detektion von SGD Standorten in Betracht gezogen werden. Im Mittelmeerraum wird der Frischwasserzufluss aus Karstgrundwasserleitern auf 75% geschätzt, wovon angenommen wird, dass ein großer Anteil submariner Grundwasserabfluss ist (Scientific Committee on Oceanic Research-Land-Ocean Interactions in the Coastal Zone, 2004). In diesem Zusammenhang ist das Ziel dieser Arbeit einen automatisierten und objektiven Ansatz zu liefern, der auf einer großräumlichen Skala thermale Satellitenbilder von Landsat 7 und Landsat 8 zur Lokalisierung von potentiellen SGD Standorten verwendet. Dieses Ziel umfasst die Entwicklung eines Algorithmus zur Wasserextraktion um nur den off-shore Bereich zu betrachten, so wie die Anpassung des Ansatzes der deskriptiven Statistik von Mallast et al. (2014) an das Mittelmeer, wo drei Standorte ausgewählt worden sind, um unterschiedliche Bedingungen und damit Durchführbarkeit für SGD Standorte zu überprüfen. Die Anpassungen beinhalten: (1) Inkludierung von Szenen mit Wolkenbedeckung um die Datenbasis zu vergrößern, (2) Implementierung von Gezeitendaten, um Ebbe-Bilder zu analysieren, da submarine Grundwasserzufluss in diesen Phasen verstärkt ist und (3) Anwendungstest von Landsat 8 Szenen, die in Zukunft die Daten liefern werden, nachdem Landsat 7 nicht mehr in Betrieb ist.

In der vorliegenden Arbeit konnte gezeigt werden, dass eine szenenbasierte Wasserextraktion notwendig ist, um akkurate Ergebnisse zu erzielen. Zu dem konnten SGD Standorte im Mittelmeerraum erfolgreich mit der Methode von Mallast et al. (2014) detektiert werden.

Schlagworte: groß-räumliche Auflösung, Landsat, Mittelmeer, submariner Grundwasserabfluss, Wasserextraktion, Wasseroberflächentemperatur

Table of Contens

1 Introduction 1

2 Study Area 3

2.1 France 3

2.2 Turkey 6

2.3 Italy 7

3 Data and Methods 9

3.1 Data and Preprocessing 9

3.2 Cloud mask 13

3.3 Water mask 15

3.4 Multi-temporal thermal analyses 17

4 Results and Discussion 21

4.1 Water mask 21

4.2 Multi-temporal thermal analyses 23

5 Conclusion and Perspective 33

References 35

Software 41

Appendix I

CD contents XV

List of Figures

1 Submarine groundwater springs in Sveti Jurjaj, Croatia 1

2 Overview of known SGD sites along the Mediterranean coast 4

3 Submarine springs between Nice, France and the French/Italian Border 5

4 Submarine springs between Kalkan and Kapakli, Turkey 7

5 Submarine discharge zones in the Lagoon of Venice, Italy 8

6 Emissivity of sea water for the wavelength 2 to 14 µm 13

7 Cloud classification in France 15

8 Calculated water indices from Landsat 8 17

9 Transects on the coast in France 18

10 Workflow of the water mask 19

11 Schematic picture of multi-temporal data 20

12 Probability distribution of the MNDWI values for a L8 and L7 scene 21

13 Relationship between T_{Otsu} and T_{Ele} 22

14 MNDWI using both literature threshold and new thresholds 23

15 Standard deviation of low tide L8 images in the Nice-Menton region, France . . . 24

16 Range and standard deviation for L8 and L7 scenes in the Cabbé region, France . 26

17 Range of low tide, atmospherically corrected L8 images in the Nice-Menton region, France 27

18 Range of low tide, atmospherically corrected L8 images in the Kalkan-Kas region, Turkey 28

19 Range of low tide, atmospherically corrected L8 images in the Lagoon of Venice, Italy 28

20 Slope of low tide, atmospherically corrected L8 images in the Nice-Menton region, France 29

21 Slope of low tide, atmospherically corrected L7 images in the Nice-Menton region, France 30

22 Slope of low tide, atmospherically corrected L8 images in the Kalkan-Kas region, Turkey 31

23 Slope of low tide, atmospherically corrected L8 images in the Lagoon of Venice, Italy. 32

24 Slope of low tide, atmospherically corrected L7 images in the Lagoon of Venice, Italy. 32

List of Tables

1 Average annual temperature and emergence characteristics of the selected study sides 3

2 Spring groups between Èze, France and the French/Italian border 5

3 Caves on the Mediterranean Rivera in south-western Turkey 6

4 Overview of bands, according wavelengths and ground sampling distance from L7 and L8 10

5 Scene Overview of the amount of scenes in the different data sets 10

6 Pre-launch temperature calibration constants and band-specific rescaling factors . 12

7 Mean sea water emissivity values 13

8 Example for both SST range and slope values for L8 low tide, atmospherically corrected images 25

List of Figures in Appendix

25 Data gaps (red) which occur through the L7 SLC failure I

26 Range and standard deviation for L8 and L7 scenes in the Kas region, Turkey . . II

27 Range and standard deviation for L8 and L7 scenes in the Lagoon of Venice, Italy . III

List of Tables in Appendix

9 Overview of known SGD sites along the Mediterranean coast IV

10 Landsat 7 auxiliary data France IX

11 Landsat 7 auxiliary data Turkey X

12 Landsat 7 auxiliary data Italy XI

13 Landsat 8 auxiliary data France XII

14 Landsat 8 auxiliary data Turkey XIII

15 Landsat 8 auxiliary data Italy XIV

List of Abbreviations

ACCA	Automatic Cloud Cover Assessment
DEM	Digital Elevation Model
DN	Digital Number
GSD	Ground Sampling Distance
L7	Landsat 7
L8	Landsat 8
Ma	Million Years
MNDWI	Modified Normilised Difference Water Index
MS	Mediterranean Sea
NaN	Not A Number
NDWI	Normilised Difference Water Index
NIR	Near Infrared
PCP	Potential Cloud Pixel
SD	Standard Deviation
SGD	Submarine Groundwater Discharge
SLC	Scan Line Corrector
SRTM	Surface Radar Topography Mission
SST	Sea Surface Temperature
SWBD	Sea Water Body Data
SWIR	Shortwave Infrared
T	Temperature
T_{Ele}	Second Threshold for MNDWI
T_{Otsu}	Threshold calculated with Otsu (1979)
TIR	Thermal Infrared
TOA	Top of Atmosphere
UAV	Unmanned Aerial Vehicle
VIS	Visible Spectrum
WFM	Water Feature Mask

1 Introduction

The increasing demand on fresh water especially during hot and dry summer months will increase the water scarcity problem e.g. in countries in the Mediterranean Sea basin (Ozyurt, 2008). Submarine groundwater discharge (SGD, Figure 1) is regarded as an important component of the hydrological cycle (International Atomic Energy Agency, 2007). The global amount of groundwater seepage is estimated to be 6 - 7% of the world's rivers which is 2 400 km^3 freshwater per year (Burnett et al., 2006). In the Mediterranean it is estimated that 75% of freshwater input is contributed from karst aquifers, wherefrom a high volume is assumed to be SGD (Scientific Committee on Oceanic Research-Land-Ocean Interactions in the Coastal Zone, 2004). In the same time SGD sites act as important pathways for nutrients and contaminants that deteriorate marine ecosystems (Slomp and Cappellen, 2004). Knowing location and discharge dynamics of SGD sites may be important information for karst groundwater utilisation which is most productive through high infiltration and transmission capacity (Ozyurt, 2008). Burnett et al. (2003) defined SGD as "any and all flow of water on continental margins from seabed to the coastal ocean, regardless of fluid composition or driving forces". The authors named two main flow components: (1) hydraulic gradient on land and (2) advective flow of recirculated seawater through permeable sediments driven by several oceanic processes. (1) is on focus in this thesis and can be defined as permanent and less variable, compared to (2) that is cycling within a small time scale (Santos et al., 2012). The hydraulic gradient is affected by tides which change the SGD rate (Burnett et al., 2003). Taniguchi (2002) showed that the flow rate is not only semi-diurnal to diurnal related to tidal changes but also to a semi-monthly variation which is caused by tidal effects of neap-spring lunar tide cycle. Through this interaction the SGD rate is decreasing with increasing tidal sea level correlated to the decreasing hydraulic head between sea level and groundwater table.

SGD sites are investigated through different methods which include stable water isotopes, naturally-occurring radioactive isotopes as well as physical and chemical parameters e.g. water temperature and salinity (Schubert et al., 2014). While isotopic measurements are mainly used to quantify groundwater flow rates, physical and chemical approaches are used to localise SGD sites. Salinity measurements are undertaken to validate located anomalies as well as to identify physico-chemical properties (Mejías et al., 2012). Schubert et al. (2014) suggested using thermal remote sensing for a pre-screening potential SGD sites in order to optimise field surveys. Although different platforms (groundbased, airborne, spaceborne) may serve for thermal remote sensing, the most cost-effective are spaceborne platforms (satellites) that likewise covers the largest spatial scale (>100 km per image).

Figure 1: Submarine groundwater springs in Sveti Jurjaj, Croatia (Horovitz, 2014).

Remote sensing has some advantages compared to in-situ measurement. Through the distance from the technical instruments to the measured object no interactions between the components are caused. That means the image shows undisturbed thermal distribution of the objects. Additionally, it is possible to measure inaccessible areas (Schultz, 1988). Handcock et al. (2006) defined three different classes of ground sampling distances (GSD), which present the distance between pixel-centres measured on the ground. The classes are defined as less than 10 m, 10 to 250 m and more than 250 m as fine, middle and coarse, respectively. Satellite images are mentioned as too coarse for stream measurements. On the other hand, airborne images (e.g. unmanned aerial vehicles (UAV) have a finer GSD but cover a smaller area (Handcock et al., 2006). One important fact of thermal images is that they show electromagnetic radiation only (Schultz, 1988). Electromagnetic radiation interacts with the surface where near infrared (NIR) and visible light (VIS) are reflected. The thermal infrared (TIR) which has a longer wavelength (3 - 14 µm) is emitted by all objects with a temperature more than 0 K (-272.15°C) (Kuenzer and Dech, 2013) and is a function of structure (material and exposition) and temperature (Sabins, 2007). Earth observation is possible in the ranges of 3 - 5 µm and 8 - 14 µm only, because in this ranges atmospheric windows, where the thermal radiation is not absorbed by the atmosphere, are present (Sabins, 2007). For thermal images mostly the range between 8 µm and 14 µm is used. In the shorter wavelengths (3 - 5 µm) an influence of sun light may influence the observation, compared to the used range where a possibility for adsorption through ozone occurs which most of the sensors can compensate. In contrast to NIR and VIS which are dependent on sunlight, TIR can be sensed during the night (Kuenzer and Dech, 2013). The remotely sensed TIR can be transferred to temperature (T) which is surface temperature only. Since it is mostly not possible to measure in-situ water temperature directly on the surface, radiation temperature and field measurements are only the same if the water column lacks a temperature gradient (Torgersen et al., 2001). Therefore it is necessary to calibrate the radiation temperature with field measurements if absolute temperatures are needed (Schultz, 1988). For some research questions only relative temperatures are required. In that case no calibration is needed (Lewandowski et al., 2013). Relative temperatures can be used as tracer for e.g. groundwater discharge detection (Mallast et al., 2013; Röper et al., 2013; Schütz and Weiler, 2011).

In this thesis TIR satellite images from Landsat 7 and Landsat 8 are used to localise known SGD sites using the approach from Mallast et al. (2014). Since the method was used at the Dead Sea with mostly clear-sky conditions, no tidal effects and a more pronounced salinity gradient between groundwater and seawater as in the Mediterranean Sea it is required to adapt this approach. This was the objective of the present thesis that includes (1) the development of an automatised and objective water extraction algorithm to focus on the offshore areas only, (2) a cloud removal to enlarge the data basis that is many times contaminated with clouds, (3) the implementation of tidal data in order to analyse low tide images as SGD is enhanced during these phases and (4) test the applicability for Landsat 8 data that will provide data in the future once Landsat 7 stops working.

2 Study Area

During the Messinian crisis ~5.96 Ma ago the Mediterranean Sea (MS) was isolated from the Atlantic Ocean. Through the fact that evaporation has been higher as surface water runoff into the MS and precipitation a large decline of sea water level was caused (Krijgsman et al., 1999). This drop of sea level causes a change in the hydraulic head therefore springs developed under the current sea level. The end of the crisis is marked with the opening of the Strait of Gibraltar (Bakalowicz, 2014). The MS was flooded within less then 20 years (Blanc, 2002) with the consequence that the submerged networks discharging groundwater into the sea via submarine springs (Fleury et al., 2007).

In order to study different conditions and hence the feasibility to derive submarine groundwater discharge (SGD) sites it was necessary to summarise known SGD spots along the Mediterranean coast (Figure 2) together with their characteristics in terms of aquifer (e.g. karstified limestone and sandstone/fluvial sediments), discharge amount and appearance (focused and diffuse) as well as emergence depth. Accounting for these different characteristics three specific study sites were chosen, that include the Côte d'Azur in France (karstified, focused SGDs, shallow emergence), the area around Antalya, Turkey (karstified, focused SGDs, deep emergence), and the Lagoon of Venice, Italy (quaternary sediments, diffuse SGDs, shallow emergence) (see Table 1).

Table 1: Average annual temperature and emergence characteristics of the selected study sides (Deutscher Wetterdienst; Climate Europe).

Location	Air temperature [°C]	Water temperature [°C]	Amount of discharge [m³/s]	Emergence	Discharge appearance
France - Nice	15	17	few - 0.2	shallow	focused
Turkey - Antalya	18.4	21	few - 0.035	deep	focused
Italy - Venice	12.7	(16 at Triest)	few	shallow	diffuse

2.1 France

Certain littoral and submarine springs are known along the 600 km French Mediterranean Coast (Durozoy and Paloc, 1967). The calcareous Arc de Nice, which is an important watershed in the Alpes-Maritimes district, receives average annual precipitation of 769 mm mainly between November and April (Deutscher Wetterdienst, 2014) and generally drains towards South. Through the marine transgression springs are below sea level with emergence depths mainly between 0 - 6 m bsl. A well-studied group of springs is the Cabbé group (No. 12). These springs are caused by the contact between Jurassic limestone of Cap-Martin and the Cretaceous marls of Roquebrune bay. The total discharge is 0.2 m³/s therefrom 0.1 m³/s discharge through a submarine, 25 m long cave (Gilli, 1999a). The group of springs is one among three main spring areas (Figure 3) which occur between Nice and Menton, discharging a total of 0.5 m³/s. Summer water temperatures are 21 - 27°C for the Mediterranean Sea and 16 - 18°C for the groundwater. The Cabbé group and Les Pissarelles (No. 20) have coastal and submarine springs which are less than 10 m offshore (Table 2). Mortola (No. 25) has a 36 m deep submarine spring with a distance of 800 m to the shoreline. Springs of Cabbé occur in 5 and 6 m depth whereas Les Pissarelles lie between 2 m asl

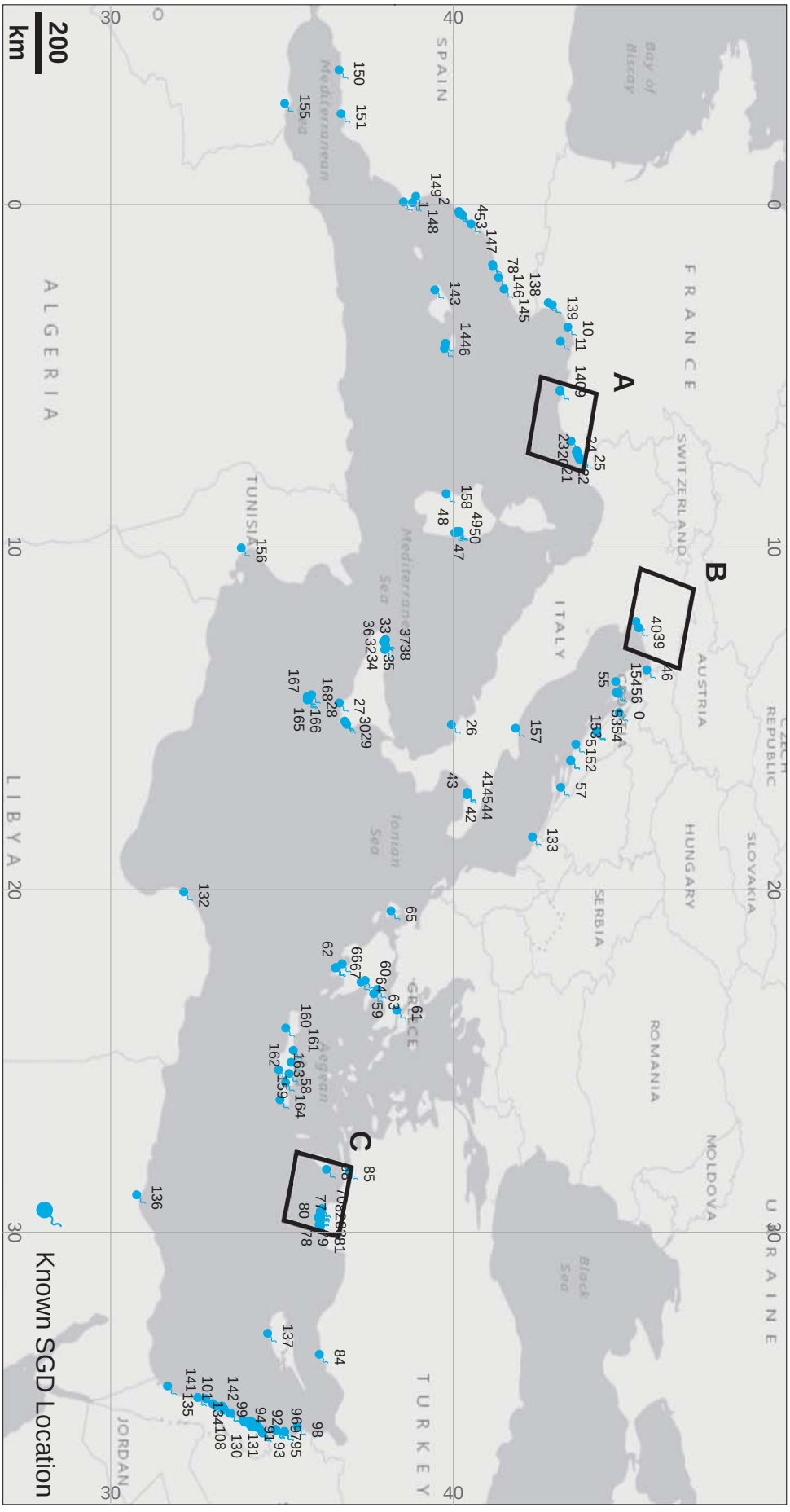

Figure 2: Overview of known SGD sites along the Mediterranean coast (numbers according to Table 9). A: Côte d'Azur, France. B: Venice Lagoon, Italy. C: Mediterranean Rivera, Turkey.

and 1 m bsl. (Gilli, 1999b). The Cabbé discharge was calculated using a hydrological water mass model which took into account precipitation, surface runoff and the volume of aquifers. During the discharge measurement an interaction between tides and the amount of discharge could be shown. During low tide a higher hydraulic gradient between coastal aquifer and sea level exists which leads to increased discharge rates in contrast to high tide periods (Tsabaris et al., 2010).

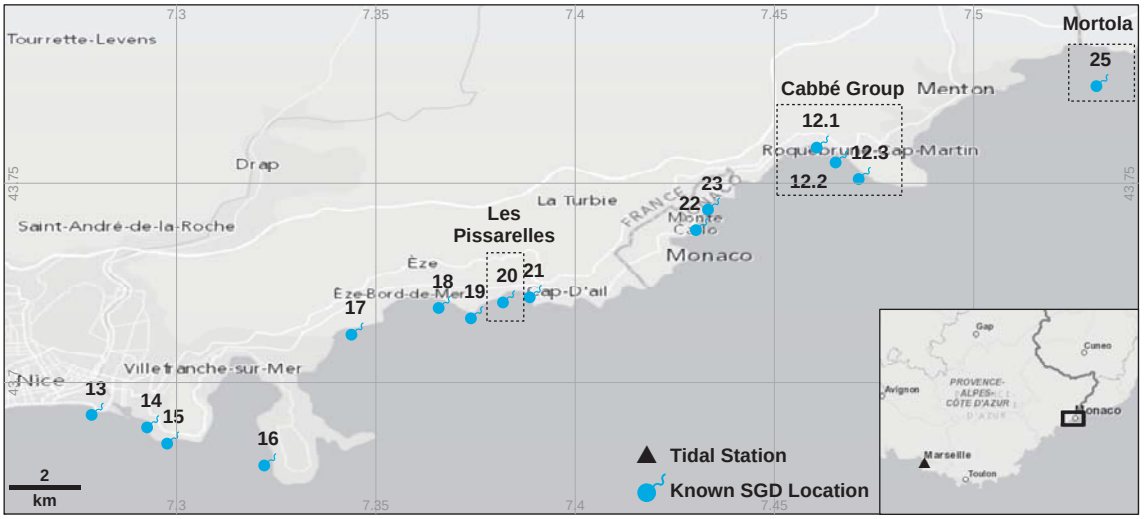

Figure 3: Submarine springs between Nice, France and the French/Italian Border. Numbers according to Table 2.

Table 2: Spring groups between Èze, France and the French/Italian border (after Gilli, 1999b).

No	Spring	Distance to shore [m]	Emergence [m msl]	Discharge volume [m³/s]
12	Cabbé Group	< 10	-5 - -6	0.2
13	Source du Château			very low
14	Source du Lazaret			very low
15	Source du Palais		-2	few
16	Source du Cap Ferrat		-6	few
17	Cap Roux			unknown (diffuse)
18	Source de l'Isolett			0.001
19	Source de Cabuel		-30	few
20	Les Pissarelles	< 10	+1 - -2	0.1
21	Source de la Mata			few
22	Pompage du Loews			0.025
23	Pompage du Larvoto			0.025
25	Mortola	800	-36	0.2

2.2 Turkey

An extremely karstified aquifer dominates the Mediterranean Rivera in south-western Turkey (Ozyurt, 2008) where 30 km behind the coastline the Taurus Mountains elevate with more than 3 000 m. Antalya receives average annual precipitation of 1078 mm (Deutscher Wetterdienst, 2014). Within a few kilometres onshore the elevation increases suddenly from sea level to 1 000 m asl. The only exceptions are coastal plains which are formed by tectonic collapse zones (Bayari et al., 2011). The entire area is dominated by carbonate rocks of Mesozoic and Tertiary ages with a well-developed karstification (Ozyurt, 2008). Bayari et al. (2011) proposed a remarkable amount of groundwater to discharge (3.6 m^3/s $\pm$50%) through SGD at numerous sites along fracture zones (Ozyurt, 2008). Although the total discharge volume includes a considerable uncertainty it provides an insight on approximate SGD volumes. Solely along a 120 km stretch of the Mediterranean coastline in the south-west of Antalya, Turkey diving surveys detected 150 SGD sites, mostly at a depth of 30 m bsl. 15 of those SGD sites origin from submarine or coastal caves with depths varying from sea surface to 40 m bsl (Table 3) (Bayari et al., 2011).

Table 3: Caves on the Mediterranean Rivera in south-western Turkey (after Bayari et al., 2011).

No	Spring	Emergence [m msl]	Discharge volume [m^3/s]
69	Patara Evleri	-1	
70	Komurluk	+2	0.035
71	Doruk	-4	
72	Prenses	-40	
73	Yilan	0	
74	Mivini	-3	
75	Havali	-4	
76	Cakil	-1	
77	Likya Batigi	0	
78	Altug	-12	0.01
79	Fakdere	-2	
80	Fok	-9	
81	Buza	-11	
82	Gokkaya	0	
83	Ilker Kaptan	-2	

At the example of the Altug cave (Figure 4 No. 78) could be shown that during the time between late autumn and mid-spring the SGD fresh-water fraction increases. As first, this time corresponds to the main rain period and second, due to the salinity variation (less saline) during the same period it becomes obvious that the hydraulic head drives the discharge being linked to recharge of the aquifer on the one hand site as well as seasonal and daily sea level change on the other (Ozyurt, 2008).

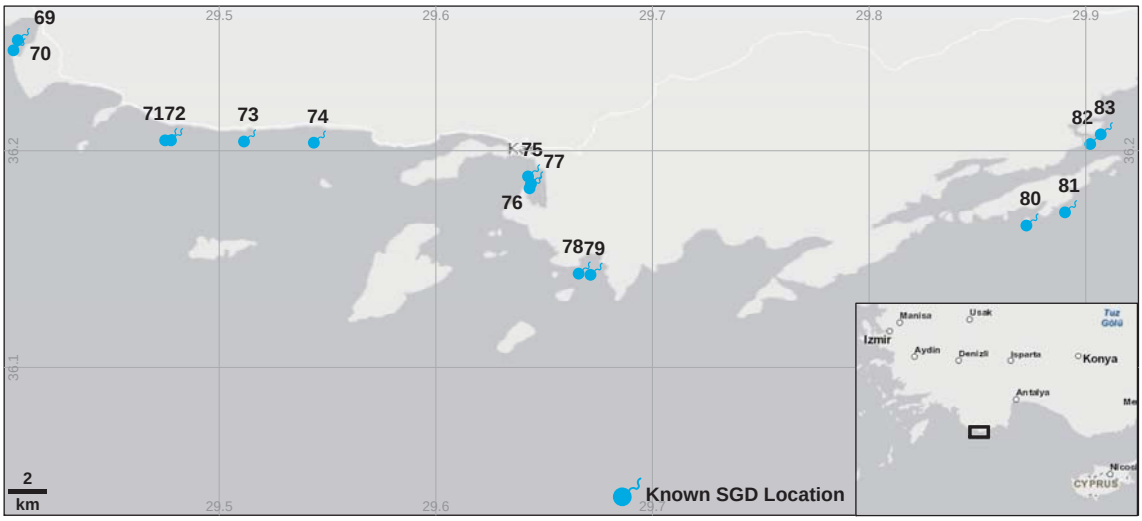

Figure 4: Submarine springs between Kalkan and Kapakli, Turkey. Numbers according to Table 3.

2.3 Italy

The lagoon of Venice, the largest in Italy, is situated in the north of the Adriatic Sea and receives average annual precipitation of 800 mm (Deutscher Wetterdienst, 2014). It covers an area of 550 km² with a length of 50 km from the North-east to the South-west and is bounded by the Sile River in the North and the Brenta River in the South. The distance between the main land and the Adriatic Sea is 8 to 14 km. The lagoon consists of shallows, tidal flats, salt marshes, islands and a net of channels. The coast which separates the Adriatic Sea from the lagoon is interrupted by three inlets (Brambati et al., 2003). The inlets provide a larger water volume than the eleven tributaries leading to a much higher salinity at the inlets (30‰) compared to the river mouths (5‰). The salinity gradient is not uniform which can be through the presence of submerged, artesian fresh water springs (Rapaglia, 2005). The Venetian area is part of the Po plain and consists mainly of Prepliocene, Pliocene and Quaternary sediments with a depth of 1000 - 5000 m. This Quaternary sediment package of alluvial and marine origin is composed of sand and silty-clay layers forming six sub-horizontal fresh water aquifers (Brambati et al., 2003). However, the topographic gradient within the last 20 km of the catchment is insignificant leading to the assumption that SGD at this spot is not dominated by hydraulic head but could be severely influenced by tidal stages (Rapaglia, 2005). Two spots of SGD (Figure 5) have been investigated by Rapaglia (2005). Isola la Cura (No. 39) is 8 km North of the City of Venice on the northern part of the lagoon. It is situated in the Canale delle Dolce which is dredged to a depth of 4 m bsl and contains coarser sediments than the rest of the lagoon. The discharge is 0.0016 m³/s through an area of 150 m². It is observed that discharge is higher at low tide than at high tide. During measurements in November the groundwater temperature differs to the lagoon water by 3°C. The second spot Fusina (No. 40) is located at the Porto Marghera Industrial zone 2 km South and 4 km West of Venice where the Naviglia Brenta Canal flows into the lagoon (Rapaglia, 2005).

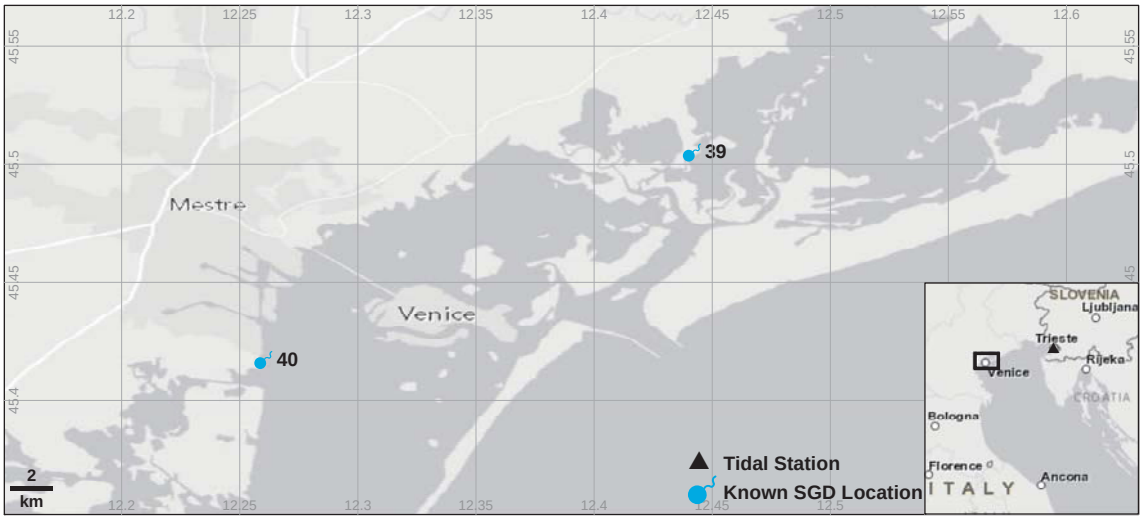

Figure 5: Submarine discharge zones in the Lagoon of Venice, Italy. Numbers according to Table 9.

3 Data and Methods

Within this section the applied data and its preprocessing to detect SGD sites are elucidated in the first subsection (3.1). The subsequent structure regards the methods applied in the sequence they were implemented. The primary aim was to integrate an already existing approach to detect and exclude clouds in images presented in subsection 3.2. This allows enlarging the data basis that so far was based on cloud-free images only. In subsection 3.3 an own approach is presented during which a water mask is developed to reduce the image to the relevant water area. Having reduced each image to the relevant and uncontaminated area, the fourth subsection (3.4) elaborates the multi-temporal analysis approaches required to detect SGD sites. The here presented method theory has been implemented within the MATLAB framework guaranteeing an automated and reproductive procedure.

3.1 Data and Preprocessing

Two satellites are used to detect SGD sites in that thesis. The older Landsat 7 (hereafter referred to as L7) and the newer Landsat 8 (hereafter referred to as L8). Both satellites have a 16 days revisit time and an orbital altitude of 705 km asl (Roy et al., 2014). L7 was launched in April 1999 and has three different ground sampling distances (GSD) of 15 m, 30 m and 60 m depending on the wavelength (bands) (National Aeronautics and Space Administration, 2010). L8 was launched in February 2013 with the same GSD as L7 except for the thermal infrared (TIR) that changed to 100 m. However, all TIR bands are resampled using a cubic convolution to 30 m (Roy et al., 2014). Compared to L7, in most cases L8 bands cover an narrower electromagnetic spectrum than the equivalent band on L7, but the new satellite has three improvements (1) an additional blue band (coastal and aerosol), (2) a third shortwave infrared band (cirrus) and (3) a second thermal infrared band (Table 4). Another important change is the radiometric resolution. While for L7 all bands are stored in an 8 bit system (256 grey values) L8 changed to a 12 bit system (4096 grey values) allowing to analyse even slighter radiation/emission changes. Additionally, all L7 scenes recorded after May 31st, 2003 exhibit missing data (~20% per scene) in form of stripes (Figure 25) due to the Scan Line Corrector (SLC) failure (U.S. Geological Survey, 2013). A calibration note from U.S. Geological Survey (2014b) suggested to avoid using band 11 from L8 through some large calibration uncertainties. Therefore band 10 will be used only to detect SGD sites.

For all three study sites between 1 - 20 L7 and L8 scenes are available provided by U.S. Geological Survey (2014c). Scenes with less than 5% cloud cover are defined as cloud free. Table 5 shows an overview of the number of cloud free and limited cloud-covered (up to 63%) scenes which are downloaded and will be used for further analyses. While the first presents an ideal basis for subsequent SGD analysis, the latter is subject to a cloud elimination approach that would enlarge the data basis. To counteract missing data due to the SLC failure regarding L7 a linear interpolation was applied to fill the data gaps. Although unavoidable, it will cause some uncertainties that will be touched in the discussion section.

USGS provides Landsat images with calibrated digital numbers (DN) which have to be converted to physically common radiometric scale e.g. reflectance for VIS - SWIR bands and brightness temperature in case of TIR bands. The procedure is slightly different for VIS-SWIR and TIR bands why both are explained separately.

Table 4: Overview of bands, according wavelengths and ground sampling distance (GSD) from L7 and L8 (note that band numbers do not correspond between both satellites, as e.g. green spectrum is covered by band 2 of L7 and band 3 of L8).

Denotation	Landsat 7			Landsat 8		
	Bands	Wavelength [µm]	GSD [m]	Bands	Wavelength [µm]	GSD [m]
Coastal and Aerosol				1	0.43 - 0.45	30
Blue	1	0.45 - 0.52	30	2	0.45 - 0.52	30
Green	2	0.53 - 0.61	30	3	0.53 - 0.60	30
Red	3	0.63 - 0.69	30	4	0.63 - 0.68	30
NIR	4	0.78 - 0.90	30	5	0.85 - 0.90	30
SWIR 1	5	1.55 - 1.75	30	6	1.56 - 1.66	30
SWIR 2	7	2.09 - 2.35	30	7	2.10 - 2.30	30
Cirrus				9	1.36 - 1.39	30
TIRS 1	6	10.4 - 12.5	60	10	10.6 - 11.2	100
TIRS 2				11	11.5 - 12.5	100
Panchromatic	8	0.52 - 0.90	15	8	0.50 - 0.68	15

Table 5: Scene Overview of the amount of scenes in the different data sets.

Location	Path	Row	Platform	available Scenes		
				Cloud free	Cloud coverage between 5 and 63%	Low tide
France	30	195	L7 SLC on	-	-	8
			L7 SLC off	6	6	
			L8	7	11	7
Italy	28	192	L7 SLC on	1	1	5
			L7 SLC off	6	12	
			L8	2	12	4
Turkey	35	179	L7 SLC on	2	-	2
			L7 SLC off	5	3	
			L8	16	2	5

Preprocessing VIS - SWIR

During the first step, all bands are first converted to at-sensor spectral radiance through band specific rescaling gain and bias factors as given in Equation 1.

$$L_\lambda = G_{rescale} \cdot Q_{cal} + B_{rescale} \quad \text{(Equation 1)}$$

where L_λ is at sensor spectral radiance [W/(m² sr µm)]
Q_{cal} is quantised calibrated pixel value [DN]
$G_{rescale}$ is band-specific rescaling gain factor [(W/(m² sr µm))/DN]
$B_{rescale}$ is band-specific rescaling bias factor [W/(m² sr µm)]
Note: $G_{rescale}$ and $B_{rescale}$ are provided in L8 metadata file as Radiance_Mult_Band_x and Radiance_Add_Band_x, respectively where x is the band number. Chander et al. (2009) provide both factors for L7 (Table 6).

Afterwards, all bands are converted to top of atmosphere (TOA) reflectance (Equation 2) in order to reduce scene-to-scene variability. This approach incorporates three advantages. (1) The cosine effect of different solar zenith angles is removed which is acquired from time difference between data acquisition. (2) Exoatmospheric solar irradiance from spectral band differences is compensated. (3) Variation of different Earth-Sun distance is corrected (Chander et al., 2009). While for L7 Equation 2 is used, the conversion to TOA reflectance for L8 does not rely on the intermediate step through Equation 1 but can be directly performed with DN as input (U.S. Geological Survey, 2014d) as given in Equation 3. Within the presented approach it is not necessary to apply an atmospheric correction for VIS-SWIR bands which is sufficient to convert DN to TOA reflectance.

$$\text{L7}: \quad \rho_\lambda = \frac{\pi \cdot L_\lambda \cdot d^2}{ESUN_\lambda \cdot \cos\theta_{SZ}} \quad \text{(Equation 2)}$$

where ρ_λ is planetary TOA reflectance
L_λ is at sensor spectral radiance [W/(m² sr µm)]
d is Earth-Sun distance [astronomical units]
$ESUN_\lambda$ is mean exoatmospheric solar irradiance [W/(m² µm)]
θ_{SZ} is solar zenith angle [degrees] which is $90° - \theta_{SE}$ where θ_{SE} is local sun elevation angle from the metadata (Sun_Elevation)

$$\text{L8}: \quad \rho_\lambda = \frac{M_P \cdot Q_{cal} \cdot A_P}{\cos\theta_{SE}} \quad \text{(Equation 3)}$$

where ρ_λ is planetary TOA reflectance
M_P is band-specific multiplicative rescaling factor from the metadata (Reflectance_Mult_Band_x, where x is the band number)
A_P is band-specific additive rescaling factor from the metadata (Reflectance_Add_Band_x, where x is the band number)
Q_{cal} is quantised calibrated pixel value [DN]
θ_{SE} is local sun elevation angle [degrees] from the metadata (Sun_Elevation)

Preprocessing TIR

Throughout the present study effective at-sensor brightness temperature and atmospherically corrected surface temperatures are an issue of investigation as direct comparison. Hence, both are presented here. Effective at-sensor brightness temperature can be directly calculated from L_λ using Equation 4 assuming the earth's surface to behave like an ideal black body and excluding any atmospheric effects.

$$T = \frac{K_2}{\ln(\frac{K_1}{L_\lambda} + 1)} \qquad \text{(Equation 4)}$$

where T is effective at-sensor brightness temperature [K]
L_λ is at sensor spectral radiance [W/(m² sr µm)]
K_2 pre-launch calibration constant 2 [K] (Table 6)
K_1 prelaunch calibration constant 1 [W/(m² sr µm)] (Table 6)

Table 6: Pre-launch temperature calibration constants needed to calculate at-sensor brightness temperature (Equation 4) and band-specific rescaling factors for Equation 1.

Platform	Band	K_1 $[\frac{W}{m^2 \cdot sr \cdot \mu m}]$	K_2 [K]	$G_{rescale}$ $[\frac{W}{m^2 \cdot sr \cdot \mu m}/DN]$	$B_{rescale}$ $[\frac{W}{m^2 \cdot sr \cdot \mu m}]$
L7	6	666.09	1282.71	0.037205	3.16
L8	10	774.89	1321.08	$3.3420 \cdot 10^{-4}$	0.1
	11	480.89	1201.14		

An atmospherically correction of TIR bands accounts for the attenuation of surface leaving thermal radiation and thermal radiation emitted from the atmosphere itself that strongly depend on atmospheric conditions (aerosol content, humidity, temperature etc.) at the specific time and place. To correct images atmospherically at sensor spectral radiance form Equation 1 has to be transferred to surface radiance of an ideal black body first, incorporating (1) scene specific up- and downwelling radiance and transmission values and (2) emissivity of the earth's surface as given in Equation 5 (Barsi et al., 2003).

$$L_T = \frac{L_\lambda - L_U - \tau \cdot (1 - \varepsilon) \cdot L_D}{\tau \cdot \varepsilon} \qquad \text{(Equation 5)}$$

where L_T is radiance of an ideal black body [W/(m² sr µm)]
L_λ is at sensor spectral radiance [W/(m² sr µm)]
L_U is upwelling radiance [W/(m² sr µm)]
L_D is downwelling radiance [W/(m² sr µm)]
ε is emissivity of the surface [-]
τ is atmospheric transmission [-]

Since it is necessary to have knowledge about transmission, upwelling and downwelling radiance of the atmosphere for the specific site and time for each scene a radiative transfer model has to

be used (Barsi et al., 2005). Barsi et al. (2003) developed a web-based atmospheric correction tool which provides transmission, upwelling and downwelling radiance of the atmosphere and is based on commercially available software MODTRAN. The emissivity of sea water (Figure 6) was calculated using the ASTER spectral library (version 2.0) (Baldridge et al., 2009). The mean emissivity value (Table 7) of the band specific wavelength was calculated and used in Equation 5.

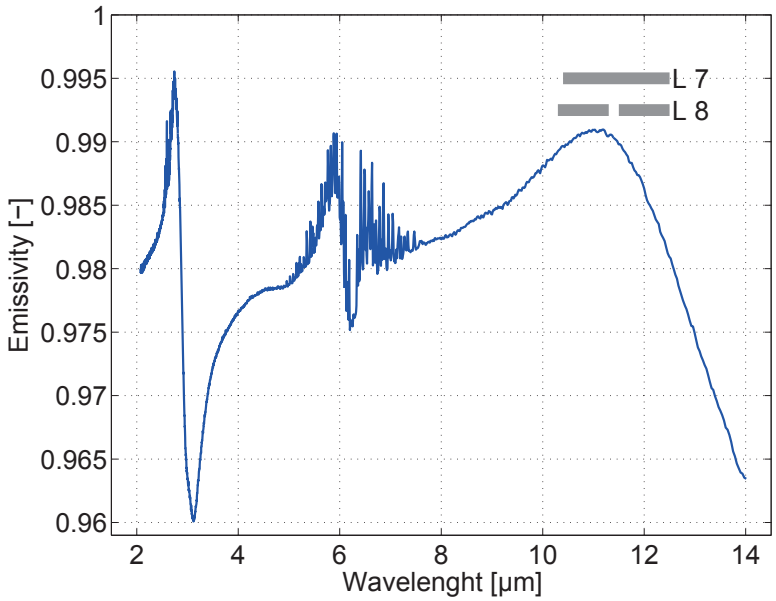

Figure 6: Emissivity of sea water for the wavelength 2 to 14 µm (Baldridge et al., 2009) as well as thermal band wavelength from L7 band 6 and L8 band 10 and band 11 indicated as grey boxes.

Table 7: Mean sea water emissivity values which has been used for atmospheric correction.

Platform	Band	Emissivity [-]
Landsat 7	6	0.9885
Landsat 8	10	0.9904
	11	0.9860

To obtain sea surface temperature (SST) the corrected radiances are input to Equation 4. The temperature error is less than 0.8 K for the temperature range of 270 - 330 K. It is noteworthy to mention that the calculated temperature represents the skin temperature (<1 mm of the uppermost water layer) which differs to the below laying bulk temperature by about 0.1 K due to sensible heat fluxes, evaporative heat loss, and long wave radiation (Wloczyk et al., 2006). This affects each scene globally and can therefore be neglected (Yokoyama et al., 1995).

3.2 Cloud mask

To extend the data volume it was necessary to integrate images with cloud cover. Since clouds are blocking or changing radiometric information leaving earth or water surface, it is most relevant to identify and exclude them. Clouds can be divided into two classes, thick opaque and thin semitransparent clouds. While thick opaque clouds can be detected through high reflectance in

the visual bands, thin clouds tend to show properties from both land/water surface and cloud. In comparison to thick opaque clouds thin semitransparent clouds are more difficult to detect (Zhu and Woodcock, 2012). A quantity of cloud cover on L7 images is provided in the metadata file. For that purpose an Automatic Cloud Cover Assessment (ACCA) is used (Irish, 2000). A multi-temporal method was introduced by Jin et al. (2013) where it is necessary to have a reference image which does not have overlapping clouds. The authors suggest that images should be acquired with a short temporal gap and within the same season. In that case cloud free images have to be chosen manually this cannot be done in an automatic process. Therefore it was necessary to choose a non multi-temporal algorithm which is provided by Zhu and Woodcock (2012). This algorithm creates a cloud probability mask using five tests including a water test. The authors provide a program which can be used to detect clouds on both type of images, L8 and L7 (Zhu, 2014a). Fmask classified clear-sky and no-clear-sky pixels into two and three different classes, respectively. Clear-sky pixels are divided into water and land pixels by using a water test. Thick clouds are classified as land because they block all information while land and water can still be identified above thin clouds. The land/water classification is mainly used for different probability calculation later. All bands are converted to TOA reflectance (section 3.1). Potential cloud pixels (PCP) are identified in pass one using four spectral tests. Pixels which are not flagged in pass one are considered as totally clear-sky pixel. To flag PCPs all four tests have to be true. If PCPs extend 99.9% of the image the second pass is skipped, otherwise clear-sky pixel and PCPs are sent to statistical analyses in pass two (Zhu and Woodcock, 2012). The Fmask was developed for TM and L7 images. According to Zhu (2014b) a new paper which includes new L8 bands, already implemented in Version 3.2.1, will be published soon. A cloud probability threshold, which has a default value of 22.5% (Zhu, 2014a), can be set by the user. After setting the threshold to different values and visually proving the results, the default threshold is used because a higher threshold changes the area of detected clouds (see blue box in Figure 7) whereas lower probability leads to wrong classification of bright features like beaches and man-made structures, marked with red boxes in Figure 7. Beside a cloud mask, Fmask also calculates a snow and a cloud shadow mask. The dilate factor was set to zero for all classes. Since the cloud class will be used only, it was not necessary to set the dilate factor for snow and cloud shadow. The factor for cloud class was set to zero because wrong clear-sky classified bright pixel (e.g. bare soil, sand and snow/ice) occur on land only which will be deleted by using water extraction. After extracting water using the water mask, discussed in 3.3, a buffer will be set to the cloud pixels.

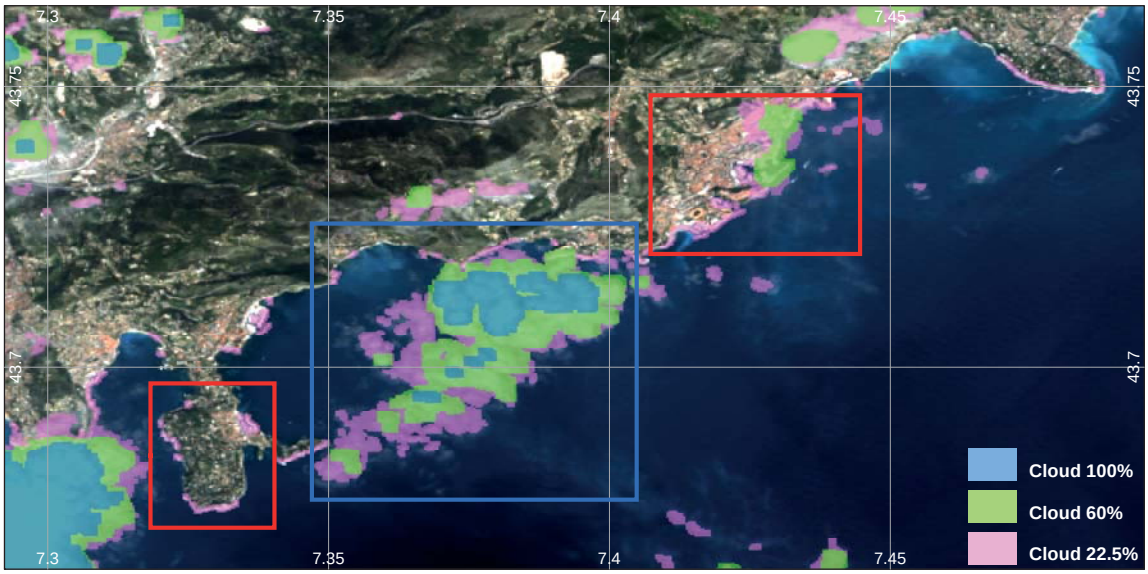

Figure 7: Cloud classification by Fmask from Zhu and Woodcock (2012) in France using different probability thresholds and a three pixel dilate factor. Red boxes show wrong classification. The blue box shows the changing cloud area for different cloud probabilities.

3.3 Water mask

A major step for multi-temporal SGD analysis is the objective and automatic water area extraction. Literature research has shown that multi-band indices, like the Normalised Difference Water Index (NDWI, Equation 6) after McFeeters (1996), are commonly used. Since water is absorbing more radiation in the near infrared (NIR) than in the green spectrum, NDWI values are positive or equal to zero. In contrast, soil and terrestrial vegetation show negative NDWI values. For that reason, McFeeters (1996) suggested zero as threshold.

$$\mathrm{NDWI} = \frac{\mathrm{GREEN} - \mathrm{NIR}}{\mathrm{GREEN} + \mathrm{NIR}} \qquad \text{(Equation 6)}$$

where GREEN is a green band of L7 and L8
NIR is a near-infrared band of L7 and L8

Xu (2006) modified the NDWI because built-up structures appear to have similar NDWI value as water structures. The author replaced the NIR by a shortwave infrared band (SWIR) in which built-up structures emit more radiation (higher reflectance) compared to green spectrum (less reflectance). The resulting Modified Normalised Difference Water Index (MNDWI, Equation 7) exhibits positive values for water and likewise excludes built-up structures as they present negative values.

$$\mathrm{MNDWI} = \frac{\mathrm{GREEN} - \mathrm{SWIR}}{\mathrm{GREEN} + \mathrm{SWIR}} \qquad \text{(Equation 7)}$$

where GREEN is a green band of L7 and L8
SWIR is a shortwave infrared band of L7 and L8

After replacing the SWIR band, the mean MNDWI value from water increased which has the effect that the contrast between water and land increased (Xu, 2006). Xu (2006) suggested to use zero as the default threshold but he showed that the value varies depending on the type of water e.g. 0.09 in case of the coastal area around Xiamen City, China for Landsat TM images. That shows that a global threshold from literature should not be used for accurate water body separation. Since the focus is on submarine groundwater discharge, which can occur quite close to the coastline, global thresholds, which are suggested in the literature, are supposed to be uncertain in this case. Furthermore, Hu et al. (2015) described the selection of thresholds as subjective and great heavy work.

After automatically calculating both water indices a land mask was separated by using 0 and 0.09 for NDWI and MNDWI, respectively. A visual inspection shows the better performance of the MNDWI for urban areas (Figure 8a) but also reveals uncertainties caused by shadow and dark forest (Figure 8b). A second approach to identify water areas was to use Sea Water Body Data (SWBD, shown in Figure 8 as blue line) which is provided by U.S. Geological Survey (2014a). This data shows next to terrestrial water bodies the seawater body which is extracted by defining zero as threshold using the global digital elevation model (DEM) of the Shuttle Radar Topography Mission (SRTM) (U.S. Geological Survey, 2005). However, although intuitive, the DEM approach is partly highly uncertain in coastal areas (Jiang et al., 2014) due to the spatial resolution (90 m) and recording method resulting in an approach to extract water areas that needs to be improved.

It was assumed that an individual threshold for each scene would show more accurate results. For that reason the combination of NDWI and MNDWI with 0 and 0.09, respectively, is used to extract a first land mask. Since snow shows higher values in the NDWI and MNDWI as 0 and 0.09, respectively, it was necessary to include a DEM. Therefore, pixels which exceed 50 m asl have been set to land because no lakes or other water features wanted to be extract but sea, which is assumed to be under 50 m asl. For each location only the scene with a minimum cloud cover in the database was used to extract a "literature land mask". The largest land area was separated and transformed to a coastline. Based on that coastline every 20^{th} pixel was chosen to generate a transect. To accomplish perpendicularity to the coast the attention was drawn to the two neighbours of the pixel. The transects (Figure 9) were generated in four different directions (0°, 45°, 90° and 135°) depending on the neighbours and a length of 51 pixel (1 coastline pixel plus 25 to each site of the coastline pixel). It was found that each transect shows two plateaus one with negative, one with positive values for land and water, respectively. A threshold was generated using the inflection point of a fitted cubic function. Since the function has shown a low coefficient of determination the method was not used to find an individual threshold. Therefore, the transects were used to create a dataset with equal number of land and water MNDWI values for each scene. Since the dataset shows a bimodal distribution, it was supposed that the MNDWI threshold would be between theses two distributions. The first approach was to fit Gaussian curves to each of the distribution and chose the point of intersection as threshold. The second method was the method according to Otsu (1979). The nonparametric and unsupervised method was developed to extract objects from their background in grey level images. Therefore, two criteria are used to find a good threshold, (1) small intraclass variance and (2) maximised variance between the two classes (Otsu, 1979). Both methods have shown good outcomes but the Otsu method performed more accurate results for land separation. Uncertainties through topographic shadow and dark forests as discussed

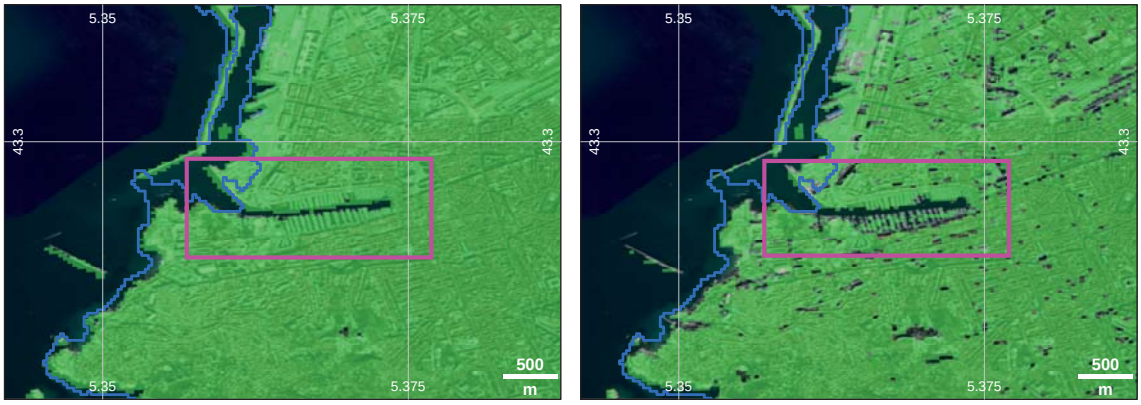

(a) left: MNDWI < 0.09 (green), right: NDWI < 0 (green). Note the data gaps in the green land area on the right show the drawbacks of using global threshold as in this case built-up structures (red box) with similar reflectance as water are included.

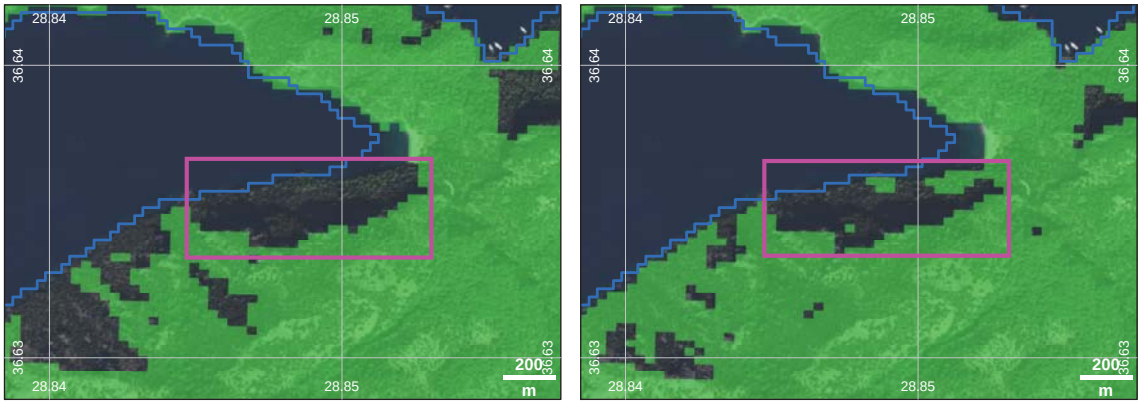

(b) left: MNDWI < 0.09 (green), right: NDWI < 0 (green). Note the data gaps in the green land area that show the drawbacks of using global threshold as in this case dark forest (red box) with similar reflectance as water are included.

Figure 8: Calculated water indices from Landsat 8: potentially true coastline indicated by SWBD (blue line).

earlier still remained. Hence, it was necessary to include the DEM. Since the spatial resolution is 90 m it was resampled to 30 m before using. The image which has been masked with the Otsu threshold (T_{Otsu}) has been divided into two classes using DEM. Water pixels where elevation is 0 m are classed as true water. A second threshold is defined as the mean MNDWI value of true water. Shadow and dark forest pixels are masked as land when they show a MNDWI value below this second threshold (T_{Ele}) and exceed 6 m asl. The result is a labelled land mask, which will be used for further analyses. Using this water mask (Figure 10) some clouds are masked as land, which is in that case not a problem because clouds as to be removed anyway.

3.4 Multi-temporal thermal analyses

After excluding clouds and land the thermal bands (band 6 and band 10 for L7 and L8, respectively) are cropped using the water feature mask (WFM) which can be used for further analyses. To reduce the runtime of the program a 5 km buffer around the coast has been set. Theoretically each pixel in an image represents a point measurement. Since scenes are taken on different times they can

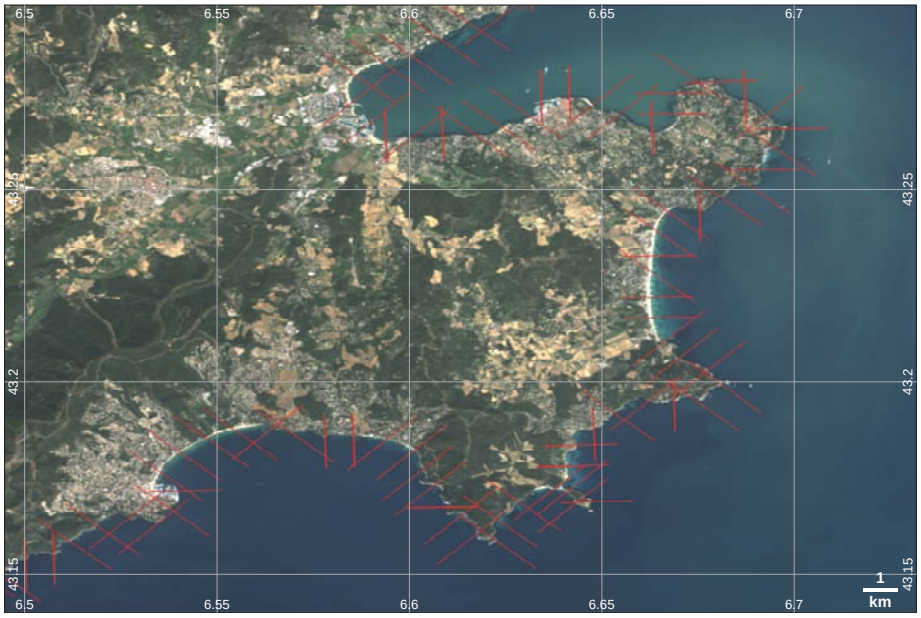

Figure 9: Transects on the coast in France.

be used as a time sequence. Therefore, it can be seen as a 3D dataset (Figure 11). For this approaches here the spatial relation between pixels is not used therefore each pixel is seen as an individual multi-temporal measurement.

In the Dead Sea, SGD sites have been detected using pixel-by-pixel descriptive statistics e.g. standard derivation (SD), range, maximum and minimum (Mallast et al., 2014). The authors have shown that SD and range can be used as indicators for groundwater discharge using sea surface temperature (SST) data series. It is assumed that groundwater tends to be less variable than surface water, which varies seasonally and daily. Through the difference in density a floating freshwater layer is formed on the Dead Sea, which stabilised the SST. Through these facts the range of groundwater influenced zones is less compared to the range of uninfluenced areas (Mallast et al., 2014). The descriptive statistic approach was tested in the area of Cabbé, France by Schubert et al. (2014). Eight L7 summer scenes have been used to indicate groundwater discharge into the Mediterranean Sea by using the standard deviation of each pixel (Schubert et al., 2014). Since the eight scenes have been chosen manually (Mallast, 2014) it was necessary to analyse the scenes to indicate why these scenes have been used. It was found that all eight scenes image a low tide situation. Additionally, Santos et al. (2009) described tidal pumping as an important factor for SGD. Therefore all multi-temporal thermal analyses have been made with low tide scenes only (Equation 8).

$$\text{low tide} = \bar{x} - 0.25 \cdot SD \qquad \text{(Equation 8)}$$

where $\bar{x}$ is the mean sea water level
SD is the standard deviation of the sea water level

Calculation time is the time span from the first Landsat image to the end of the tidal data. Satellite images on a data gap in the tidal data are not used. To compare times from both,

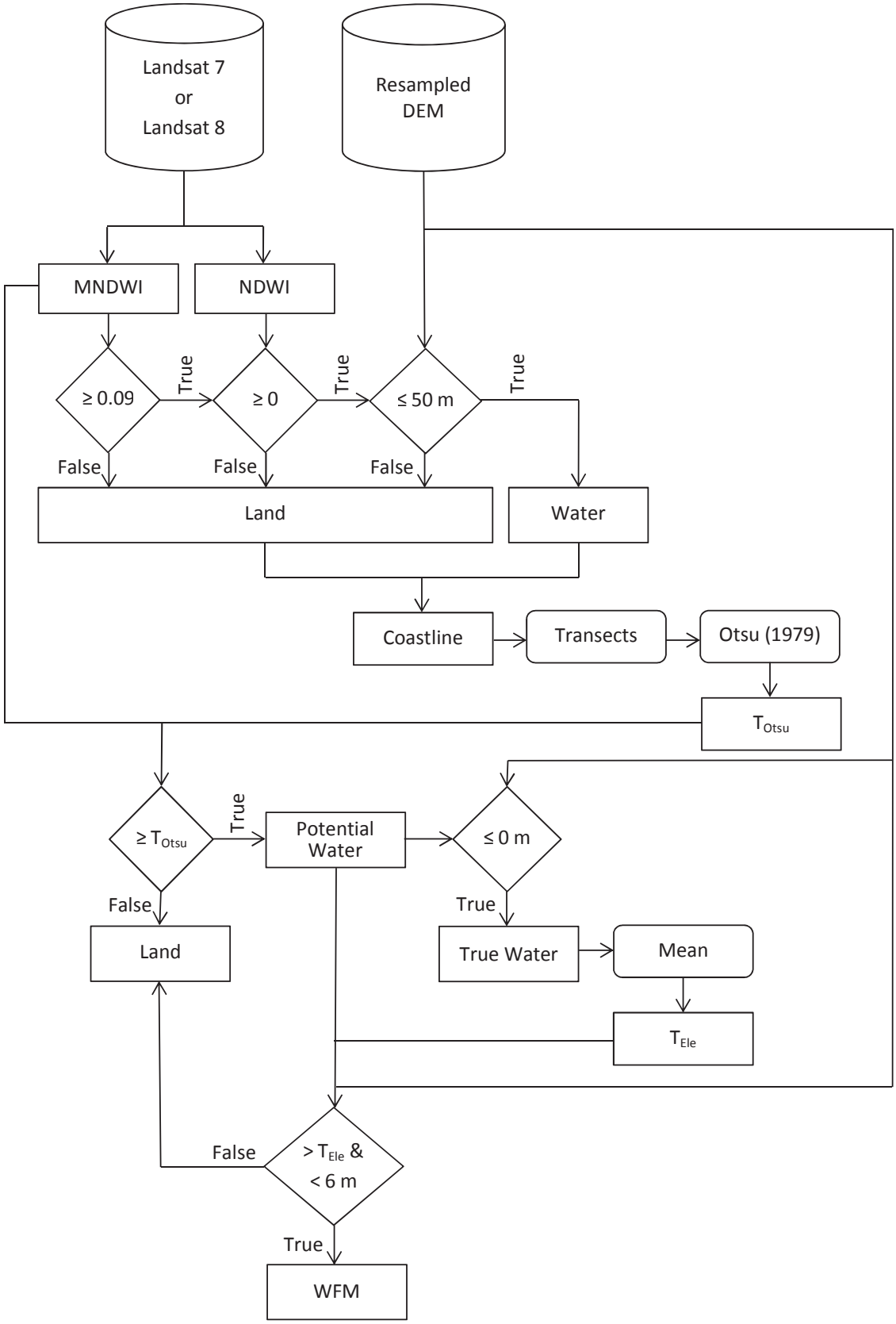

Figure 10: Workflow of the water mask.

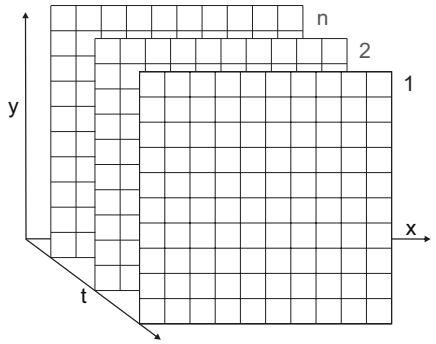

Figure 11: Schematic picture of multi-temporal data.

thermal images and tidal data, it was necessary to set both times to the full hour. The tidal dataset was downloaded from the Hawaii Sea Level Center (2014) wherefrom the nearest tidal station to the Landsat image was selected. The tidal station in Marseille and Trieste could be used for France and Italy, respectively. In the case of Turkey the nearest tidal station is Alexandria, Egypt.

Since the range is manly shaped from two scenes (minimum and maximum) the SGD site detection depends on these two scenes. Therefore a new approach was used. Since it is assumed that SST is stabilised by the groundwater, the slope of a linear model fitted to sorted SST per pixel would be less steep than the slope of the surrounding area. To fit a robust model a bootstrapping with a number of runs determined by a sensitivity analysis was used. The linear function was built by using the mean of variables generated by each bootstrap run. For the analyses more than four or 75% of all low tide scene must have a SST measurement, otherwise the slope for that pixel is not calculated and flagged as not a number (NaN).

4 Results and Discussion

In this section the results from section 3.3 (Water mask) and 3.4 (Multi-temporal thermal analyses) are shown and discussed. Since the cloud mask was used as a program the results are not further analysed.

4.1 Water mask

Through transects perpendicular to the coast a dataset with an equal number of MNDWI values for water and land was created. The threshold for the MNDWI has been calculated using the Otsu method. Figure 12 shows a representative probability distribution for both L8 (right) and L7 (left) as well as T_{Otsu} and the intraclass variance. Both probability distributions show a bimodal distribution which was expected since the dataset contains land and water values in the same amount. The L8 scene values range less (-0.3 - 0.25) for both water and land MNDWI values in contrast to the L7 scene (-0.3 - 0.8). Therefore the probability distribution is less for both surface types in the L7 dataset. The intraclass variance for water and land in the L8 scene is smaller compared to the L7 scene. That shows, additionally to the range, that MNDWI values in the L8 scene are less variable, especially for water values.

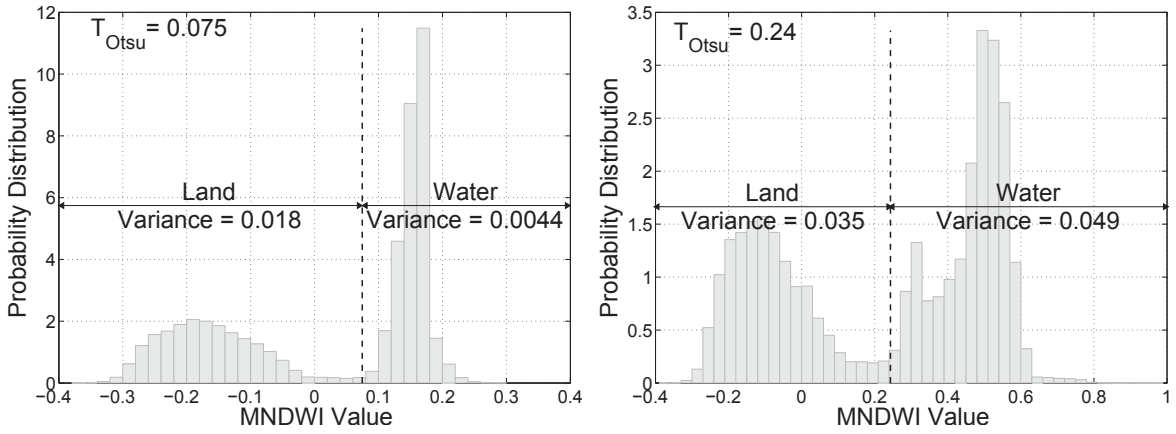

Figure 12: Probability distribution of the MNDWI values selected using transects perpendicular to the literature coastline for a L8 (left) and L7 (right) scene as well as T_{Otsu} and the intraclass variance.

In total, the new MNDWI thresholds (T_{Otsu}) show a range from 0.05 - 0.13 and 0.2 - 0.33 for L8 and L7, respectively. While the mean of the L8 T_{Otsu} (0.0825) is nearly the used threshold (0.09) from Xu (2006), the mean for the L7 scenes is much higher (0.25). Neither is close to the suggested global threshold (zero). The difference between the L7 and L8 T_{Otsu} values could be caused by a slight divergence in the average reflectance of each band between the L7 and L8 sensors which leads to -0.15 as average difference between L7 and L8 MNDWI values (Li et al., 2014). That shows that the global threshold (zero), which was suggested for L7, varies and should be adjusted to both L8 and L7.

In Figure 13 T_{Otsu} and T_{Ele} are plotted against each other, it shows that thresholds are variable depending on the location. The T_{Otsu} values for both sensors in Italy show higher values compared to France and Turkey, which show similar values. The difference could be lead to the low sea water level which causes a higher reflectance in VIS. Since the lagoon appears greenish on natural

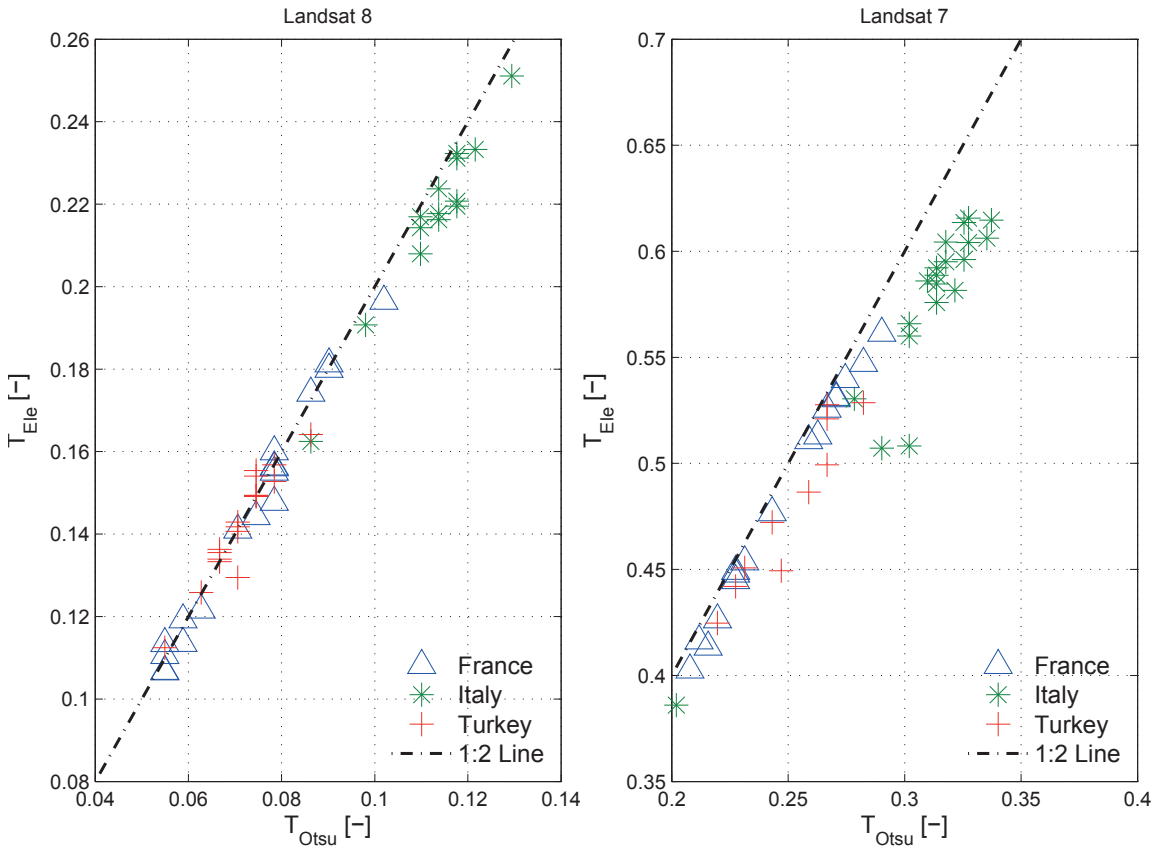

Figure 13: Relationship between calculated MNDWI threshold (T_{Otsu}) and second MNDWI threshold (T_{Ele}) which is defined as the mean MNDWI value of true water (water with an elevation of 0 m).

colour satellite images it can be assumed that higher reflectance in the green band, which is used calculating the MNDWI, cause higher MNDWI values. The plotted points are oriented on a 1:2 line while the second threshold (T_{Ele}) calculated using DEM is double of T_{Otsu}. The location itself appears to have significant influence on the distribution. France and Turkey threshold values lie on the 1:2 line, the Italy values are shifted towards T_{Otsu}. The changing values depend on local properties show once more that thresholds should be calculated individually per scene. Additionally to the fact that Xu (2006) selected the threshold (0.09) based on one L7 only.

Figure 14 shows the resulting WFM created with zero (dark green) and 0.09 (dark and light green) as thresholds as well as the WFM based on T_{Otsu} and T_{Ele}. The suggested global threshold (zero) shows large uncertainties which can be reduced by setting the threshold to 0.09. However, as discussed in section 3.3 dark forest and shadows caused by topography are still classified as water. The new method including the second threshold (T_{Ele}) sets the dark forest pixel to land and hence is advantageous.

Through the uncertainties of the SRTM as discussed in section 3.3, a few pixels are set to land which was expected. The new approach to calculate an objective and individual threshold per scene can be seen as major step forwards to automatic separation from sea water and land. Specially for environments with a changing coast e.g. through sea level changes, like in the Lagoon of Venice, where a static coastline as well as a global threshold for any water index, as it was shown, would cause high uncertainties.

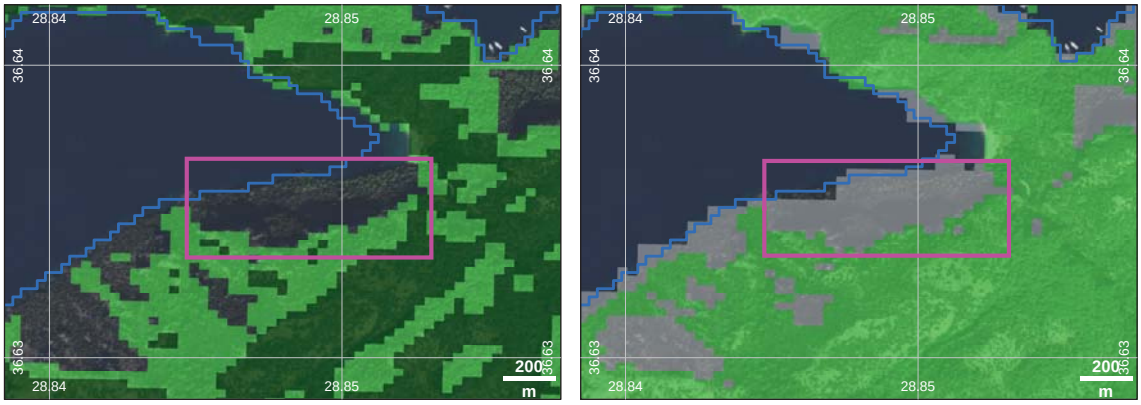

Figure 14: left: MNDWI < 0.09 (dark and light green) as well as MNDWI < 0 (dark green), the red box indicates the drawbacks of using global threshold as in this case dark forest.
right: MNDWI $< T_{Otsu}$ (green) and MNDWI $< T_{Ele}$ (grey) the red box indicates the same area as in the left figure which is improved through the second threshold. The potentially true coastline indicated by SWBD (blue line).

4.2 Multi-temporal thermal analyses

For thermal analyses the water feature mask (WFM) which was generated using the water and cloud mask was implemented to the thermal band for each scene. The first aim was to prove if an atmospheric correction is needed to detect SGD sites using satellite images. Therefore Figure 15 shows both, atmospheric corrected and not corrected standard deviation for the same area in France. It can be seen that the SGD spots are more pronounced in the atmospheric corrected image, even Cabbé 12.2 and 12.3 can be detected which is not possible in the uncorrected scene. This shows that the influences from the atmosphere which are reduced by the atmosphere correction affect the SST in each image and therefore the standard deviation (SD) of SST. Hence, all thermal scenes have been corrected atmospherically for further analyses. The resulting, atmospherically corrected images have been used to calculate pixel by pixel range and SD. Since it was shown by Schubert et al. (2014) that the SD worked for low tide scenes, two datasets (all available scenes and low tide scenes) has been used for calculation. Figure 15a shows the low tide SD for the selected area in France using L8 images. It can be seen that data gaps resulting from the cloud mask and boundary effects from clouds influence the results. Therefore the Cabbé region (B), where a cloud uninfluenced region and known SGD sites with different flow rates are present, was chosen to compare the two different methods as well as L7 and L8 images. In the Nice region (A) two SGD sites can be seen but the volume of discharge is unknown. Additionally, the Source du Lazaret (No. 14) is probable affected by the harbour of Nice where SST is stabilised through shipping. The influences of the clouds do not allow to set a focus on other discharge area shown in Figure 3. Therefore Figure 16 presents the results for the two methods (range and SD) and the different datasets (all and low tide) in the Cabbé region, France.

In Figure 16 A and B as well as in E and F all L8 and L7 scenes, respectively, are processed. On the L8 images (A and B) Cabbé 1 (No. 12.1) can be seen but none of the two other discharge sites. Since Cabbé 1 has a lower amount of discharge than Cabbé 2 the SST is less stabilised by Cabbé 2 which could be either through cloud boundary effects or differences in the bathymetry

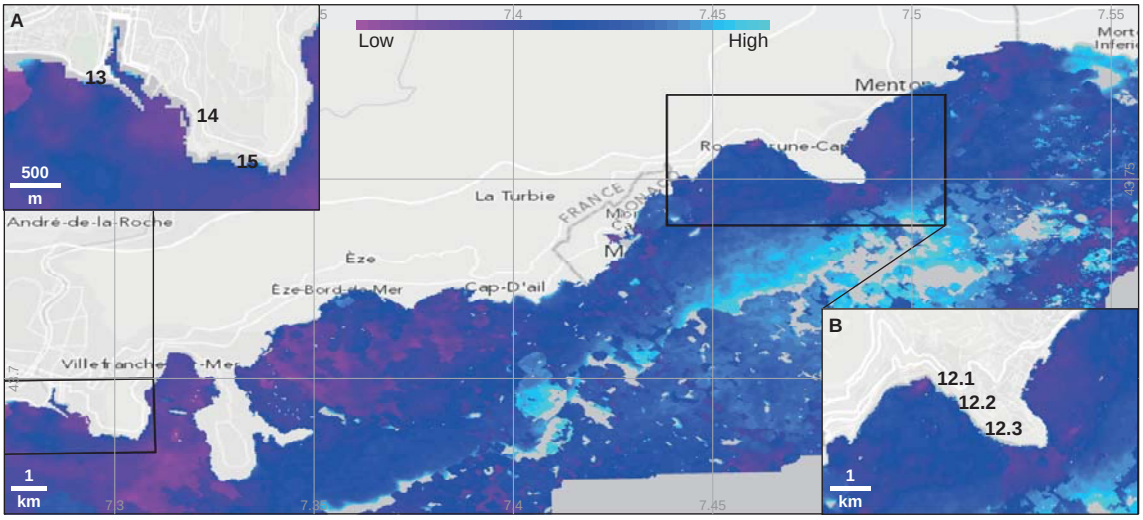

(a) Standard deviation of low tide, atmospherically corrected L8 images in the Nice-Menton region, France. Numbers are according to Table 2.

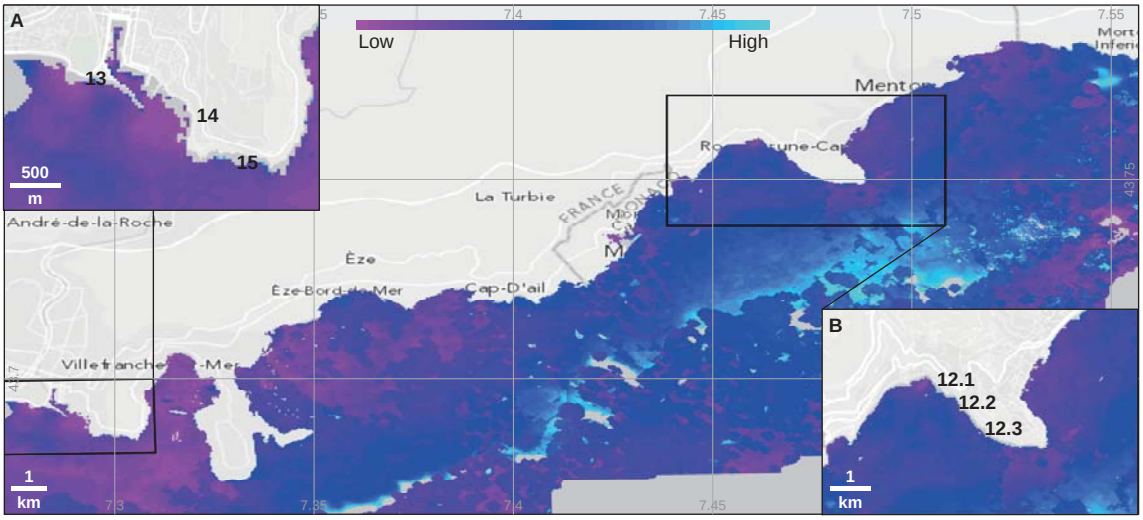

(b) Standard deviation of low tide, not atmospherically corrected L8 images in the Nice-Menton region, France. Numbers are according to Table 2.

Figure 15: Standard deviation of low tide L8 images in the Nice-Menton region, France.

(beach and steep coast). The border to the coast has high range and SD values which could be caused by differences in the sea surface level. Additionally, tidal variability was mentioned as main SGD driver by Burnett et al. (2003). Therefore, low tide scenes have been used only. The results are shown in Figure 16 C and D where all three discharge zones can be seen. Figure 16 D shows some drawbacks on the southern part of the peninsula Cap-Martin which is caused by some clouds. Both methods show a low range and low SD in the east of the peninsula. Gilli (1999b) showed that three rivers discharge into the Mediterranean Sea east of Cap-Martin in the drainage area alluvial deposits occur. These deposits can cause diffuse discharge which stabilise the SST and therefore show a low range and standard deviation. Neither, variability in Figure 16 show a typical surface runoff plume which are caused by streams nor natural colour satellite images show evidence of the streams therefore it is thought that the volume of surface discharge is not relevant. Since the range image is less cloud affected it was analysed for all known discharge areas shown in Figure 3.

Compared to the L8 variability, L7 does not show any of the known SGD sites in Figure 16 E and F whereas G and H show low variability on spots where no SGD is known. It is assumed that this spots are caused by the SLC failure data gaps (Figure 25) because the spots occur in line as well as equal distances. Additionally, there is more noise compared to the L8 images which is an evidence of the different storage system (8 bits compared to 12 bits).

Absolute values cannot be compared between the study sites because they are related to surrounding environment (Table 8). Therefore both methods are discussed relative to each other.

Table 8: Example for both SST range and slope values for L8 low tide, atmospherically corrected images.

Site	Range			Slope		
	SGD	No SGD	Mediterranean Sea	SGD	No SGD	Mediterranean Sea
France	9.85	11.40	12.27	1.94	2.30	2.56
Turkey	5.53	7.16	8.24	2.13	2.80	3.16
Italy	11.74	12.96	12.09	3.96	4.72	4.37

The above discussed findings show that atmospherically corrected, low tide, range images present undisturbed results. Same results could be seen in Turkey (Figure 26) and Italy (Figure 27).

Analyses of the SST range

Figure 17 shows the range for low tide, atmospherically corrected L8 scenes in the region between Nice and Menton, France. The totally sheltered bays show a lower variability compared to the more exposed margins which can be seen as an indication that the values should be read as relative to the surrounding area. Again, the Cabbé sites (Figure 17 B) can be detected as well as the diffuse discharge through the alluvial deposits on the western site of the peninsula Cap-Martin. Cabbé 1 shows a large area where the SST range is small. Since the shape of that zone is drawing a curve, it is supposed to be influenced through a sea current. Furthermore, two out of three sources in the Nice area (A) can be identified. Since the amount of discharging groundwater on this spots is low (Gilli, 1999a) it is assumed that SST is stabilised through some other effects than groundwater input. In case of Source du Lazaret (No. 14) it could be that the harbour is influencing through

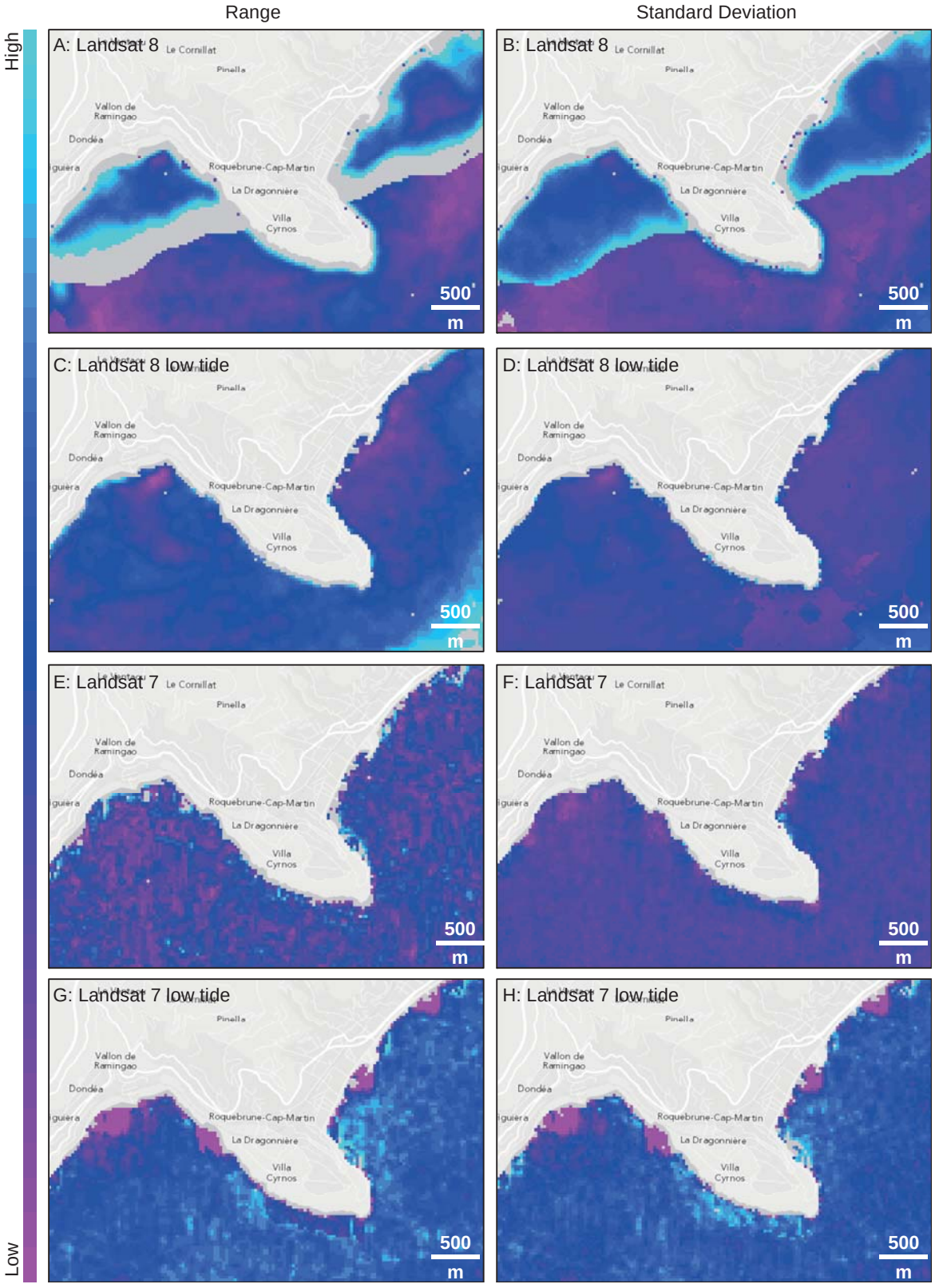

Figure 16: Overview of Range (left column) and standard deviation (right column) for L8 and L7 scenes using either all available thermal scenes or low tide scenes, in the Cabbé region, France.

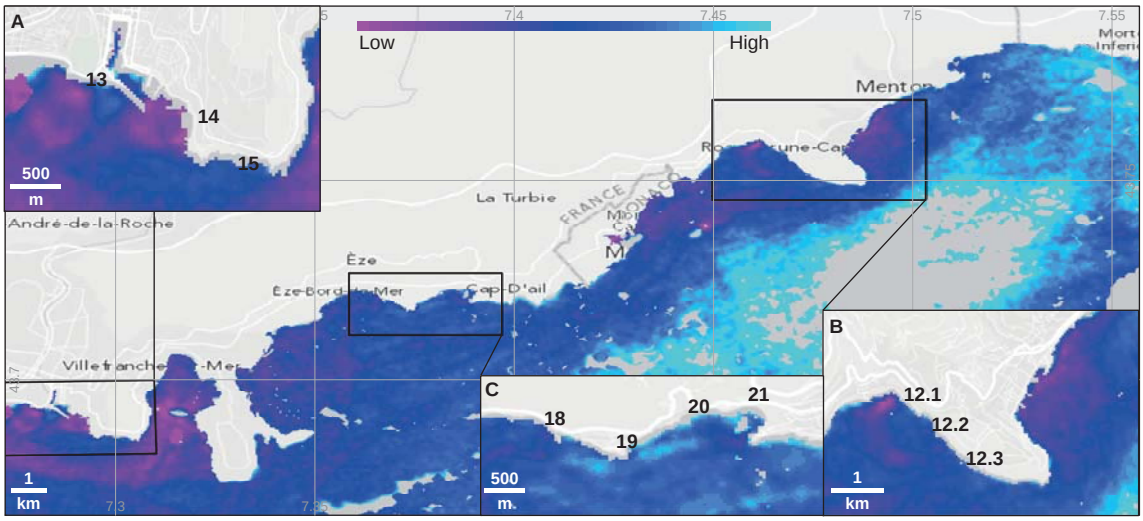

Figure 17: Range of low tide, atmospherically corrected L8 images in the Nice-Menton region, France. Numbers are according to Table 2.

shipping. In the area around Èze (C) two spots with a low range can be seen. One is around the known Source de l'Isolette (No. 18) where 1 l/s discharge into the Mediterranean Sea. The discharge volume is low compared to Les Pissarelles (No. 20, 100 l/s) which does not show a low SST range spot. The second spot is not known as SGD site. As a consequence of sea currents Les Pissarelles could appear ~400 m south-west of the known emergence.

As discussed above in the Kas-Kalkan region the SGD sites have different emergence characteristics compared to these in France. As it can be seen in Figure 18 some spots show a low SST range which can be seen as possible discharge spots. Since they are not lying on the known locations it is considered that sea currents redirect the groundwater flow. Bayari et al. (2011) described the caves, where the groundwater flow originate, as coastal caves but the provided coordinates do not point on a coastal region which can be caused through rounding of the coordinates. Figure 18 A shows a spot in the north of the bay which could be the Patara Evleri (No. 69) the plume suggested a large amount of discharging groundwater, compared to Komurluk (No. 70) in the south-east where only a few pixel show a low SST range. Since the emergence of Komurluk is 2 m asl it is supposed to be on the coastline. Figure 18 B is situated in a bay, like Figure 17 B. Again the low SST range spots do not fit to the known spots. The largest spot in the north of the bay is presumed to be the Havali cave with a 4 m bsl emergence. Since the spot is wide spread a current can stabilise SST using the groundwater emerging from the cave. The two other known submarine caves in that bay have less pronounced signals. Figure 18 C shows a location exposed to the Mediterranean Sea in contrast to the two which are located in a bay. Therefore, in the total image it can be seen that the area C has a higher SST range compared to the two other sites. Doruk (No. 71) and Prenses (No. 72) do not show a low SST range spot, since Prenses has an emergence depth of 40 m bsl it is assumed that the signal, if any, would be low especially in that exposed area. Since the locations are supposed to be on the shoreline the low SST range spot east of Yilan (No. 73) could be seen as SGD spot. The other low range spots with some distance to the shoreline show a widespread signal which is typical for a diffuse discharge near the shoreline. Since no discharge volume is known it is uncertain to identify this spots as SGD sites rather it can be seen as potential

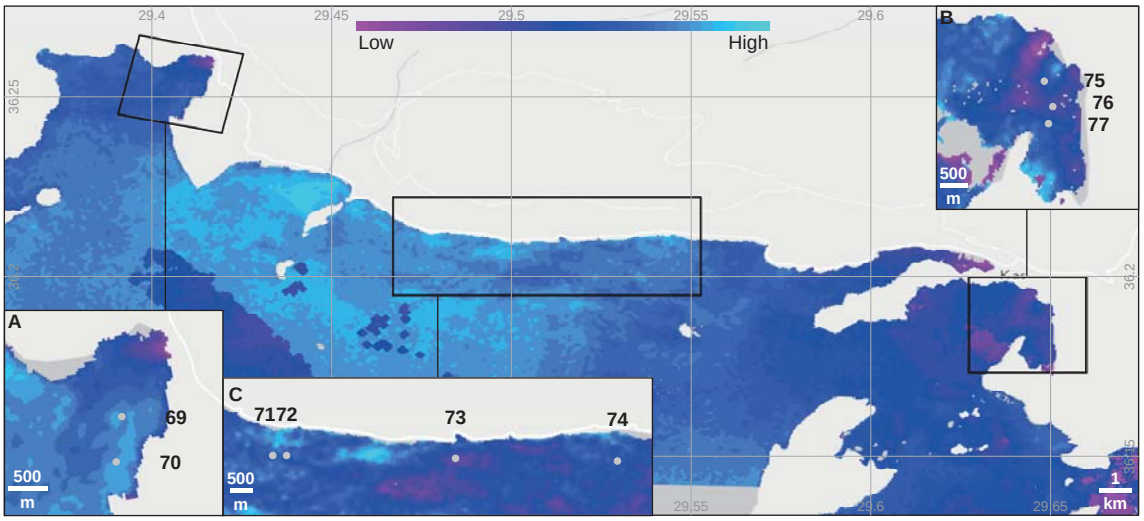

Figure 18: Range of low tide, atmospherically corrected L8 images in the Kalkan-Kas region, Turkey. Numbers are according to Table 3.

discharge spot.

Figure 19 shows the Lagoon of Venice in Italy where two diffuse discharge spots are known. In total the SST range is medium to high with the exception of the part south of Venice where the SST range less, compared to other parts of the lagoon. Figure 19 A shows the Fusina (No. 40) discharge area. At the known location the range of the SST is higher compared to the surrounding area. South of this spot two low range patches are present. The smaller one is probably caused by the river which is discharging into the Lagoon. The region further south seems like a diffuse discharge area occurring through the sediments. Figure 19 B where the discharge location of Isola la Cura (No. 39) occurs, no specific low SST range zone can be localised, since the SST in the focused spot appears to be in the same range as the surrounding.

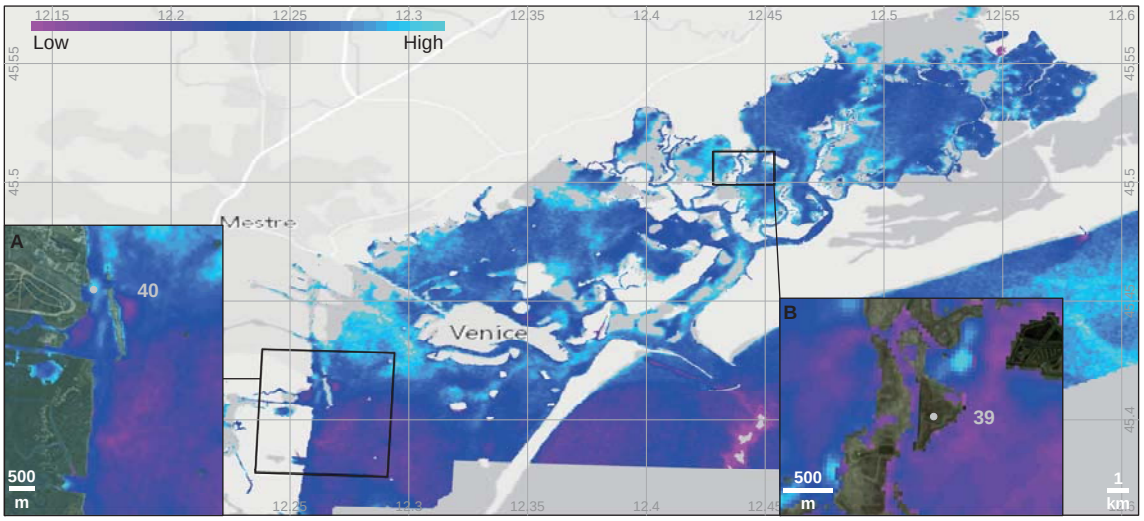

Figure 19: Range of low tide, atmospherically corrected L8 images in the Lagoon of Venice, Italy. Numbers are according to Table 9.

Analyses of the slope

Since range is mainly created from two scenes (minimum and maximum) the slope of a pixel based linear bootstrapped function is analysed. As discussed above low tide, atmospherically corrected thermal images have been used. To compare the results with the SST range method the same SGD sites are focused on. Figure 20 shows the slope values in the Nice-Menton region for L8 low tide images. On the first glance the image shows an inhomogeneous picture which is caused by cutting clouds out, showing the same pattern as Figure 15a. Analyses of individual pixels have shown, that the slope is influenced by SST which have a small difference to each other. That effect would have an influence on all multi-temporal pixel functions, since some pixels are excluded by the cloud mask not all functions are affected. This "plateau effect" caused the inhomogeneous image. However, the SGD sites in Cabbé (Figure 20 B) can be detected. As it was mentioned before, Cabbé 1 (No. 12.1) shows a larger stabilised area as Cabbé 2. The potential diffuse discharge zone east of the peninsula Cap-Martin can be seen as well as the drawbacks from the cloud mask in the south of the peninsula. Figure 20 A images the two SGD sites in Nice compared to the low tide SST range image (Figure 17 A) the zones are smaller and more pronounced. In contrast to Figure 20 B, where the range of the slope values is 0.75 (1.85 - 2.6), Figure 20 A has a range from 0.3 (1.7 - 2) only. Which can be a consequence of the low discharge volume. The small discharge is stabilising the SST less compared to the surrounding not groundwater influenced zone. The Cabbé sites have a large discharge volume therefore the slope values have a higher contrast to the MS water. Through the removed cloud pixels the discharge zones in Figure 20 C cannot be discussed.

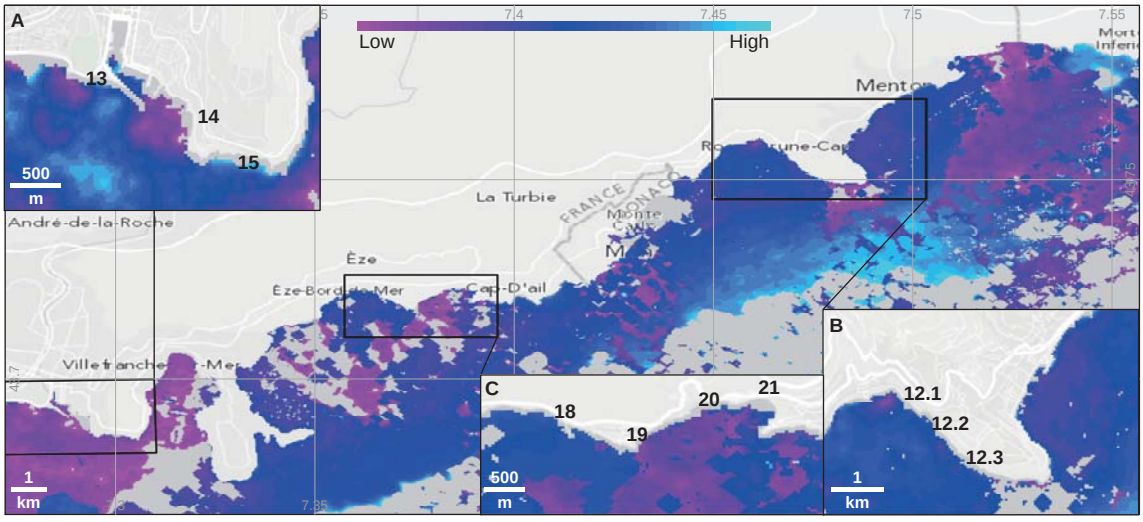

Figure 20: Slope of low tide, atmospherically corrected L8 images in the Nice-Menton region, France. Numbers are according to Table 2.

Figure 21 shows the slope values for low tide, atmospherically corrected L7 scenes. Since the available scenes are taken in summer only, the image does not show any of the known SGD sites which shows that both seasons must be considered to get reliable results. Another reason can be that discharge was too low during the time of the thermal images and therefore no SST signal was given. To make sure that discharge occurs it should be tested if precipitation data can be included. The small slope values are again caused by the SLC failure which was already shown in

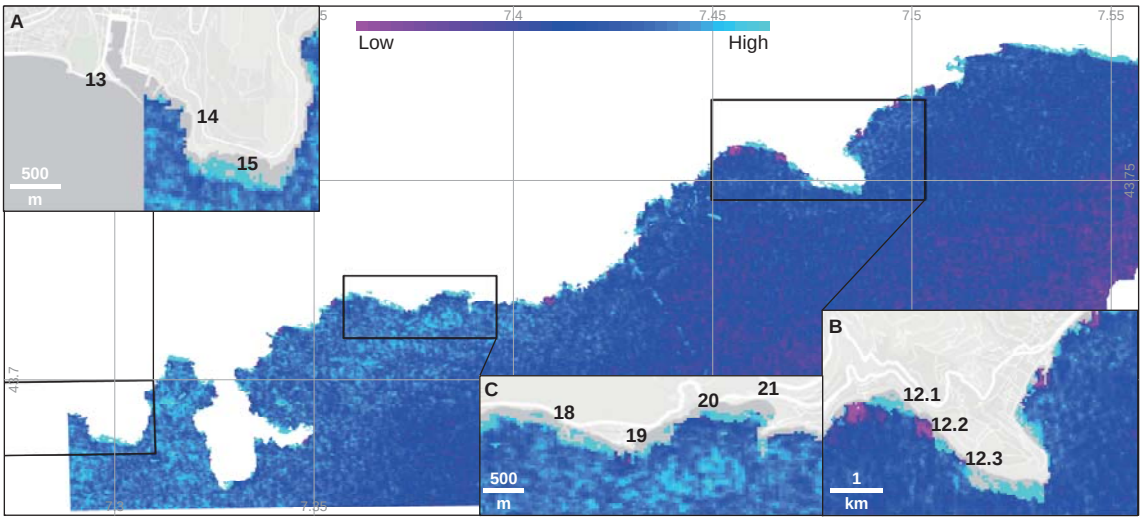

Figure 21: Slope of low tide, atmospherically corrected L7 images in the Nice-Menton region, France. Numbers are according to Table 2.

Figure 16 G and H. The image (Figure 21) shows that the MS SST is more stabilised than the SST close to the shoreline.

Figure 22 shows the slope values in the Kalkan-Kas region, Turkey. Since five low tide scenes have been available only, data gaps are produced through the condition that a slope is calculated only if four scenes or 75% of the data contain valid SST. Nevertheless, the three discharge points already seen in the SST range image (Figure 18) show a less rising slope compared to the surrounding (Figure 22 B). Additionally, a zone with a small slope can be seen in the west of the bay which could represent a diffuse discharge area. Bayari and Ozyurt (2007) illustrated that area as a proven site for freshwater discharge. In Figure 22 A none of the SGD site can be seen because of the "plateau effect" which is caused by a difference in the amount of scenes. Figure 22 C shows small slope values in the region of Yilan (No. 73) and Mivini (No. 74) as it was discussed for the SST range the SGD site are situated highly exposed to the Mediterranean Sea therefore currents can widespread the groundwater and reduce the variability of the SST over a wider area and more offshore as the caves occur. The L7 slope for the region could not be analysed since there have been two low tide scenes only.

The slope analyses in the Lagoon of Venice calculated using four thermal images show a less variable area in the south of Venice (Figure 23). While the northern part shows a data gap because less than four pictures have shown SST measurements, the Isola de la Cura (No. 39) does not show any results. Compared to the SST range in Figure 19 the patterns are similar. The small slope values around Fusina (No. 40) are most probable caused by the surface runoff which is discharging into the lagoon. The same results can be seen in Figure 24 where five L7 images have been used to calculate a linear function. Since more low tide scenes have been available the region around the Isola de la Cura (No. 39) could be analysed. The site is known as diffuse discharge where a wider area is affected by discharging groundwater than it is expected for focused SGD sites. Figure 24 B shows some zones with a small slope. On the west side of the island the less variable area is ~400 m from the shoreline. As already observed by Rapaglia (2005) the discharge farther from the island has a larger volume as in a fewer distance to the island.

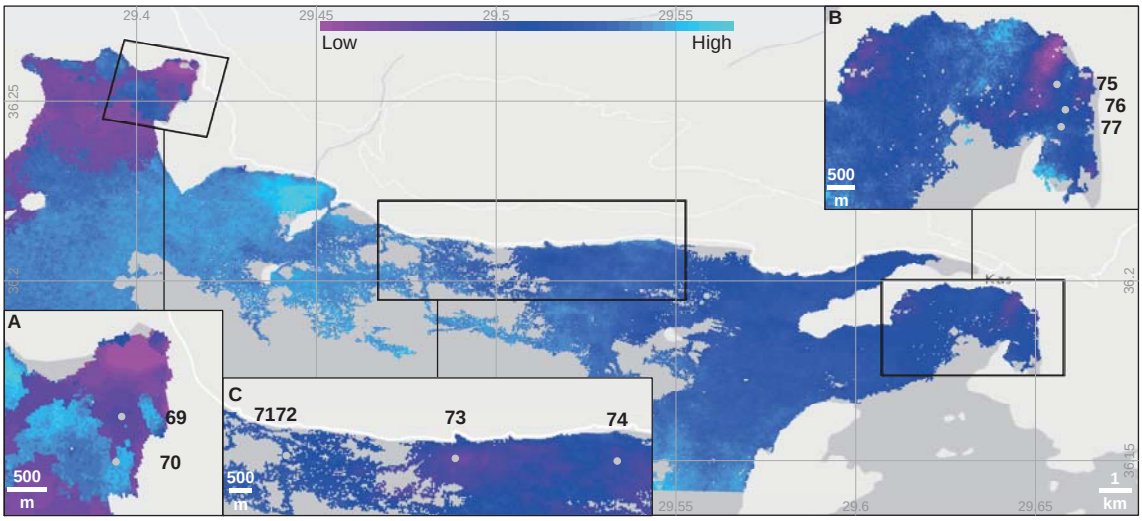

Figure 22: Slope of low tide, atmospherically corrected L8 images in the Kalkan-Kas region, Turkey. Numbers are according to Table 3.

Discussion of the SD and slope method

Both methods show the same known SGD sites. While L7 results are influenced through the interpolation which was necessary through the SLC failure, the L8 outcome was affected by fewer images available which caused data gaps especially for the slope method. Nevertheless, known SGD sites could be detected. It was seen that sites with a high discharge volume near the coastline show more prominent signals than discharge zones with a small discharge volume or deeper emergence. Additionally, the differences between groundwater unaffected SST and groundwater discharge influenced SST slope values are higher on SGD sites with a higher discharge volume compared to sites with a low discharge volume. Bayari et al. (2011) described diver detected SGD sites with a spatial resolution of 10 - 20 m while the ground sampling distance is 60 m and 100 m for L7 and L8, respectively. Hence, low discharge sites cannot be sensed using satellite images through the small stabilised SST zones. However, both types of discharge (diffuse and focused) can be detected using both methods. Few SGD spots have been displaced on the satellite images compared to the known spots which could be caused by sea currents. This aspect has to be proven in further field investigations. The SD and slope method show the same drawbacks caused by clouds. Since the range of the SST is mostly influenced by all maximum and minimum of the scenes, the slope approach can be seen as a more representative method using all scenes. However, the removed cloud pixel has to be accomplished to improve the method by reducing the "plateau effect". It may be that a larger amount of scenes will reduce this effect. A major impact on the results could be made by using low tide scenes only. Since the method using descriptive statistic parameter was implemented in the Dead Sea area (Mallast et al., 2014) in that case it was not required to take tidal cycles into account. Therefore, the method could be successfully adapted to the Mediterranean Sea.

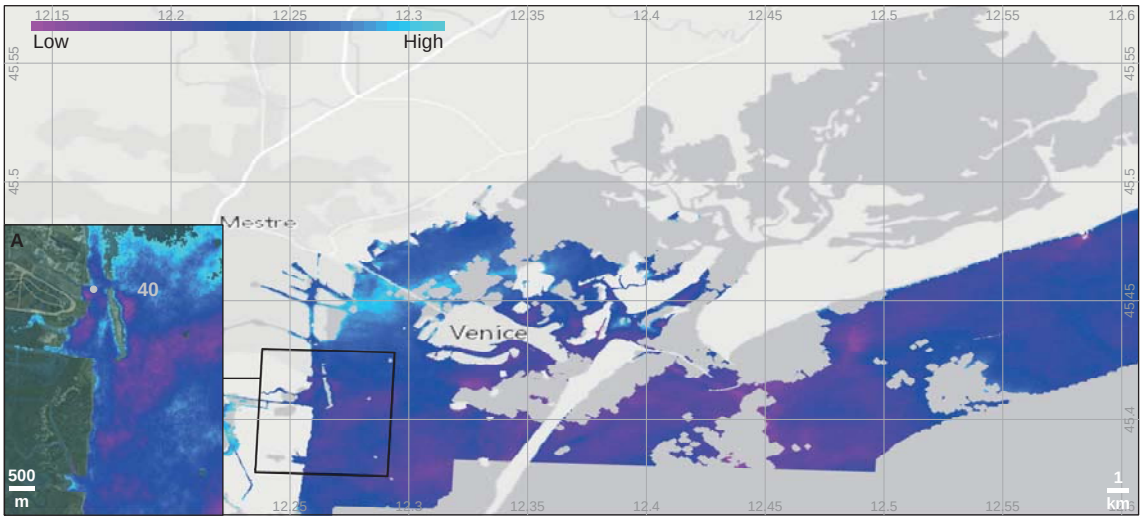

Figure 23: Slope of low tide, atmospherically corrected L8 images in the Lagoon of Venice, Italy. Numbers according to Table 9.

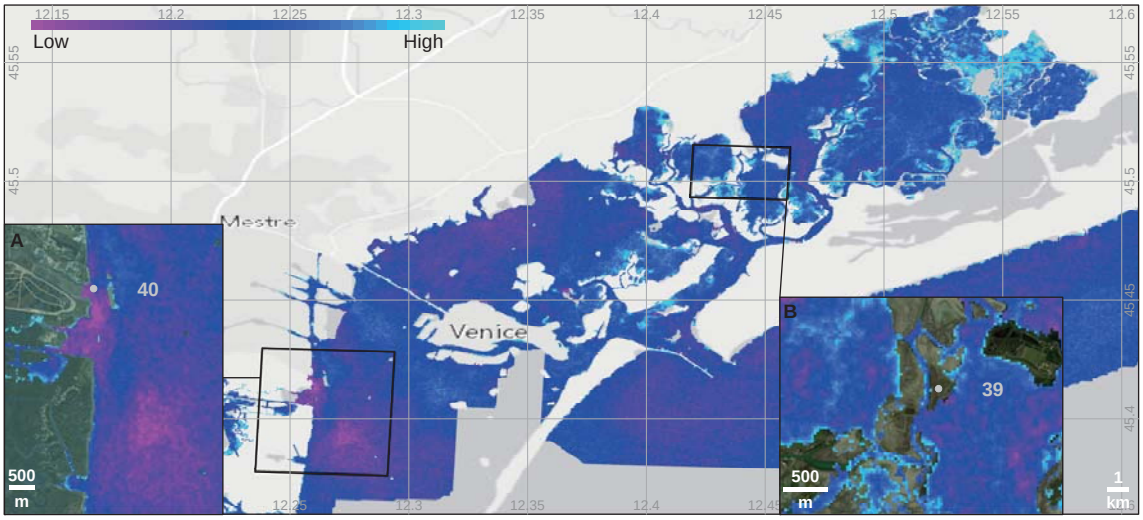

Figure 24: Slope of low tide, atmospherically corrected L7 images in the Lagoon of Venice, Italy. Numbers according to Table 9.

5 Conclusion and Perspective

The own approach for an objective water mask can be considered as method to automatically separate sea water and land features. It could be shown that the threshold which was defined as global threshold by Xu (2006) shows high uncertainties. Since the author already used a different threshold than the global an automatically approach was needed to calculate an individual threshold for L7 and L8 images. Using the individual threshold uncertainties remain especially in dark forest and shadow caused by topography. Therefore a second threshold was included that depends on the DEM. Due to the coarse GSD of the DEM some misclassification are caused which should be improved. Through the use of DEM thresholds during the process the method can be used to extract sea water only. Since the transects are calculated for the largest land area separated from the literature coastline there may be problems where small islands occur only. Further work should be focused on the possibility to extract lakes and streams as well as reducing uncertainties caused by the DEM and calculating transects for every land area. Nevertheless, the method makes a major effort towards an automatically and objective water extraction.

In the second part has focused on the submarine groundwater discharge detection using multi-temporal thermal analyses. The method using descriptive statistic parameter specially range and standard deviation by Mallast et al. (2014) was adapted to the Mediterranean Sea. Since the method was developed for the Dead Sea were satellite images with cloud cover are rare and no sea level change occurs through tidal cycles it was essential to adapt the method to a region where tidal cycles occur and cloud cover is more frequent. While the SD method showed drawbacks caused by data gaps, the range method showed more homogeneous results. However, both methods could be used to detect SGD sites regardless to the discharge characteristics (diffuse and focused) exceptions are deep emergence. Better results could be shown in bays compared to more exposed sites. To adapt the methods to the Mediterranean Sea it was necessary to exclude high tide images. Excluding the data gaps caused by clouds it was supposed that the slope of a bootstrapped linear regression function reduces this effect. However, effects caused by data gaps could not be removed through this approach but it shows similar results compared to the range method. Since a restricted number of thermal images have been available it is theorised that a larger amount of scenes will be remove the effect. Additionally, the exclusion of high tide scenes and data gaps in the Landsat 7 images caused by SLC failure reduces the number of images and pixels, respectively. Since images are still taken from both sensors the data base is growing which is important especially in case of Landsat 8. Another option could be to develop a factor which makes the slope values independent from the amount of scenes. An additional finding was, that atmospheric correction is recommended before using the methods. Including scenes with a cloud cover, the database was extended but the unequal number of pixels causes different values in the multi-temporal analyses. Therefore, a more robust method is needed.

Further studies should focus on the selection of scenes which could be improved through the low tide images. Nevertheless, precipitation data which is influencing groundwater discharge could be implemented. Since the reaction on precipitation is depending on the aquifer further information must be provided. Therefore the simply approach to detect SGD sites would become more complex. No matter which method is used, for a global approach relative values must be converted to absolute values. One idea is to take the interception from the linear function into account.

Additionally, the form of the stabilised SST area can be helpful to exclude sites which are affected through other influences. It should be proved if sea currents are influencing the pattern or location of stabilised SST through SGD. To detect SGD sites with a smaller discharge amount images with a smaller ground sampling distances are recommended. Furthermore, these images are suitable for smaller hydrological units like lakes and surface runoff systems. Since satellites image the earth continuously they can be considered as a reliable source for thermal images. Nevertheless, the free of charge policy for Landsat images makes it a possible data source for a first localisation of SGD sites for most of the globe. Even the size of localised spots could be a first estimation for the significance of discharging water as potential resource for water as well as nutrient and contaminant input to the sea. Further analyses of quantity and quality are needed to evaluate particular SGD sites as potential supplier of fresh or grey water.

References

Bakalowicz, M., 2014. Karst at depth below the sea level around the Mediterranean due to the Messinian crisis of salinitay. Hydrogeological consequences and issues. Geologica Belgica 17 (1), 96–101.

Baldridge, A. M., Hook, S. J., Grove, C. I., Rivera, G., 2009. The ASTER spectral library version 2.0. Remote Sensing of Environment 113 (4), 711–715.

Barsi, J. A., Barker, J. L., Schott, J. R., 2003. An Atmospheric Correction Parameter Calculator for a single thermal band earth-sensing instrument. In: IGARSS 2003. 2003 IEEE International Geoscience and Remote Sensing Symposium. pp. 3014–3016.

Barsi, J. A., Schott, J. R., Palluconi, F. D., Hook, S. J., Butler, J. J., 2005. Validation of a Web-Based Atmospheric Correction Tool for Single Thermal Band Instruments. Proceedings of SPIE (5882).

Bayari, S. C., Ozyurt, N. N., 2007. Isotopic and chemical characterization of coastal and submarine karstic groundwater discharges in southern Turkey. In: International Atomic Energy Agency (Ed.), Nuclear and Isotopic Techniques for the Characterization of Submarine Groundwater Discharge in Coastal Zones. pp. 75–91.

Bayari, S. C., Ozyurt, N. N., Oztan, M., Bastanlar, Y., Varinlioglu, G., Koyuncu, H., Ulkenli, H., Hamarat, S., 2011. Submarine and coastal karstic groundwater discharges along the southwestern Mediterranean coast of Turkey. Hydrogeology Journal 19 (2), 399–414.

Blanc, P.-L., 2002. The opening of the Plio-Quaternary Gibraltar Strait: assessing the size of a cataclysm. Geodinamica Acta 15 (5-6), 303–317.

Bonacci, O., Fritz, F., Denic, V., 1995. Hydrolgeology of Slanac Spring, Croatia. Hydrogeology Journal 3 (3), 31–40.

Brambati, A., Carbognin, L., Quaia, T., Teatini, P., Tosi, L., 2003. The Lagoon of Venice: geological setting, evolution and land subsidence. Episodes 2003 (26/3), 264–268.

Burnett, W. C., Aggarwal, P. K., Aureli, A., Bokuniewicz, H., Cable, J. E., Charette, M. A., Kontar, E., Krupa, S., Kulkarni, K. M., Loveless, A., Moore, W. S., Oberdorfer, J. A., Oliveira, J., Ozyurt, N. N., Povinec, P., Privitera, A., Rajar, R., Ramessur, R. T., Scholten, J., Stieglitz, T., Taniguchi, M., Turner, J. V., 2006. Quantifying submarine groundwater discharge in the coastal zone via multiple methods. Science of the Total Environment 367 (2-3), 498–543.

Burnett, W. C., Bokuniewicz, H., Huettel, M., Moore, W. S., Taniguchi, M., 2003. Groundwater and pore water inputs to the coastal zone. Biogeochemistry 66 (1/2), 3–33.

Cassinis, R., 1967. Detection of Fresh Water Submarine Flows by Means of Insitu Salinity Measurements of Sea Water. La Ricerca Scientifica 37 (3).

Chander, G., Markham, B. L., Helder, D. L., 2009. Summary of current radiometric calibration coefficients for Landsat MSS, TM, ETM+, and EO-1 ALI sensors. Remote Sensing of Environment 113 (5), 893–903.

Charideh, A., Rahman, A., 2007. Environmental isotopic and hydrochemical study of water in the karst aquifer and submarine springs of the Syrian coast. Hydrogeology Journal 15 (2), 351–364.

Climate Europe, 2014. Climate Europe.
URL http://climatedata.eu/continent.php?cid=150&lang=en

Deutscher Wetterdienst, 2014. Wetter und Klima - Deutscher Wetterdienst – Klimadaten.
URL http://www.dwd.de/bvbw/appmanager/bvbw/dwdwwwDesktop?_nfpb=true&_pageLabel=_dwdwww_klima_umwelt_klimadaten_deutschland&T82002gsbDocumentPath=Navigation%2FOeffentlichkeit%2FKlima__Umwelt%2FKlimadaten%2Fkldaten__kostenfrei%2Fkldiagramme__node.html%3F__nnn%3Dtrue

Durozoy, G., Paloc, H., 1967. Recherches sur les ressources en eaux karstiques du littoral méditerranéen Francais.

El-Gamal, A. A., Peterson, R. N., Burnett, W. C., 2012. Detecting Freshwater Inputs via Groundwater Discharge to Marina Lagoon, Mediterranean Coast, Egypt. Estuaries and Coasts 35 (6), 1486–1499.

Elhatip, H., 2003. The Use of Hydrocemical Techniques to Estimate the Discharge of Ovacik Submarine Springs on the Mediterraenean Coast of Turkey. Environmental Geology (43), 714–719.

European Cooperation in the Field of Scientific and Technical Research, 2005. Groundwater Management of Coastal Karstic Aquifers: Final Report.

Fleury, P., 2005. Sources Sous-Marines et Aquiferes Karstiques Côtiers Mediterraneens. Fonctionnement et Caracterisation: These de Doctorat.

Fleury, P., Bakalowicz, M., de Marsily, G., 2007. Submarine springs and coastal karst aquifers: A review. Journal of Hydrology 339 (1-2), 79–92.

Food and Agriculture Organization of the United Nations, 1964. Karst Groundwater Investigations Greece.

Garcia-Solsona, E., Garcia-Orellana, J., Masqué, P., Garcés, E., Radakovitch, O., Mayer, A., Estradé, S., Basterretxea, G., 2010. An assessment of karstic submarine groundwater and associated nutrient discharge to a Mediterranean coastal area (Balearic Islands, Spain) using radium isotopes. Biogeochemistry 97 (2-3), 211–229.

Gilli, E., 1999a. Détection de sources sous-marines et précision de l'impluvium par mesure des variations de salinité. L'exemple de la source de Cabbé-Massolins (Roquebrune-Cap-Martin, France). Comptes Rendus de l'Académie des Sciences - Series IIA - Earth and Planetary Science 329 (2), 109–116.

Gilli, E., 1999b. Inventaire des émergences karstiques littorales et sous-marines des Alpes-Maritimes (France). Captage expérimental de Cabbé. Annales du Museum d'histoire naturelle de Nice (14), 77–89.

Handcock, R. N., Gillespie, A. R., Cherkauer, K. A., Kay, J. E., Burges, S. J., Kampf, S. K., 2006. Accuracy and uncertainty of thermal-infrared remote sensing of stream temperatures at multiple spatial scales. Remote Sensing of Environment 100 (4), 427–440.

Hawaii Sea Level Center, 2014. Sea Level Data.
URL http://uhslc.soest.hawaii.edu/thredds/uhslc_fast_hourly.html

Horovitz, M., 2014. Submarine groundwater springs in Sveti Jurjaj, Croatia: personal correspondence.

Hu, Y.-x., Huang, J.-l., Du, Y., Han, P.-p., Wang, J.-l., Huang, W., 2015. Monitoring wetland vegetation pattern response to water-level change resulting from the Three Gorges Project in the two largest freshwater lakes of China. Ecological Engineering 74, 274–285.

International Atomic Energy Agency, 2007. Nuclear and Isotopic Techniques for the Characterization of Submarine Groundwater Discharge in Coastal Zones: Results of a coordinated research project 2001–2006.

Irish, R. R., 2000. Landsat 7 automatic cloud cover assessment. In: AeroSense 2000. pp. 348–355.

Jiang, H., Feng, M., Zhu, Y., Lu, N., Huang, J., Xiao, T., 2014. An Automated Method for Extracting Rivers and Lakes from Landsat Imagery. Remote Sensing 6 (6), 5067–5089.

Jin, S., Homer, C., Yang, L., Xian, G., Fry, J., Danielson, P., Townsend, P. A., 2013. Automated cloud and shadow detection and filling using two-date Landsat imagery in the USA. International Journal of Remote Sensing 34 (5), 1540–1560.

Kohout, F. A., 1966. Submarine Springs a Neglected Phenomenon of Coastal Hydrology.

Krijgsman, W., Hilgen, F. J., Raffi, I., Sierro, F. J., Wilson, D. S., 1999. Chronology, causes and progression of the Messinian salinity crisis. Nature (400), 652–655.

Kuenzer, C., Dech, S., 2013. Theoretical background of thermal infrared remote sensing. In: Kuenzer, C. (Ed.), Thermal infrared remote sensing: Sensors, methods, applications. Springer, pp. 1–26.

Kuhta, M., 2004. Vrana Lake on Cres Island - Genesis, Characteristics and Prospects. In: Proceedings of the XXXIII Congress IAH & 7th Congress ALHSUD: Groundwater Flow Understanding from Local to Regional Scales.

Lewandowski, J., Meinikmann, K., Ruhtz, T., Pöschke, F., Kirillin, G., 2013. Localization of lacustrine groundwater discharge (LGD) by airborne measurement of thermal infrared radiation. Remote Sensing of Environment 138, 119–125.

Li, P., Jiang, L., Feng, Z., 2014. Cross-Comparison of Vegetation Indices Derived from Landsat-7 Enhanced Thematic Mapper Plus (ETM+) and Landsat-8 Operational Land Imager (OLI) Sensors. Remote Sensing 6 (1), 310–329.

Mallast, U., 2014. Choice of Landsat scenes in Cabbé, France: personal correspondence.

Mallast, U., Gloaguen, R., Friesen, J., Rödiger, T., Geyer, S., Merz, R., Siebert, C., 2014. How to identify groundwater-caused thermal anomalies in lakes based on multi-temporal satellite data in semi-arid regions. Hydrology and Earth System Sciences 18 (7), 2773–2787.

Mallast, U., Siebert, C., Wagner, B., Sauter, M., Gloaguen, R., Geyer, S., Merz, R., 2013. Localisation and temporal variability of groundwater discharge into the Dead Sea using thermal satellite data. Environmental Earth Sciences 69 (2), 587–603.

Mandel, S., Gilboa, Y., Mercado, A., 1972. Groundwater Flow in Calcareous Aquifers in the Vicinity of Barcelona, Spain. Hydrological Sciences Bulletin 17 (1), 77–83.

Marinos, P., Herman, J. S., Back, W., Xidakis, G., 1985. Structural Control and Geomorphic Significant of Groundwater Discharge Along the Coast of the Mani Penisul, Peleponnese, Greece. Karst Water Resources (Proceedings of the Ankara - Antalya Symposium).

Matić, N., Miklavčić, I., Maldini, K., Tomas, D., Cuculić, V., Cardellini, C., Frančišković-Bilinski, S., 2013. Geochemical and isotopic characteristics of karstic springs in coastal mountains (Southern Croatia). Journal of Geochemical Exploration 132, 90–110.

McFeeters, S. K., 1996. The use of Normalized Difference Water Index (NDWI) in the delineation of open water features. International Journal of Remote Sensing 7 (17), 1425–1432.

Mejías, M., Ballesteros, B. J., Antón-Pacheco, C., Domínguez, J. A., Garcia-Orellana, J., Garcia-Solsona, E., Masqué, P., 2012. Methodological study of submarine groundwater discharge from a karstic aquifer in the Western Mediterranean Sea. Journal of Hydrology 464-465, 27–40.

National Aeronautics and Space Administration, 2010. Landsat 7 Science Data Users Handbook. URL `http://landsathandbook.gsfc.nasa.gov/pdfs/Landsat7_Handbook.pdf`

Ollivier, P., Claude, C., Radakovitch, O., Hamelin, B., 2008. TIMS measurements of 226Ra and 228Ra in the Gulf of Lion, an attempt to quantify submarine groundwater discharge. Marine Chemistry 109 (3-4), 337–354.

Otsu, N., 1979. A Threshold Selection Method from Grey-Level Histograms. Transections on Systems, Man, and Cybernetics 9 (1), 62–66.

Ozyurt, N. N., 2008. Analysis of drivers governing temporal salinity and temperature variations in groundwater discharge from Altug Submarine Karst Cave (Kas-Turkey). Environmental Geology 54 (4), 731–736.

Potié, L., Ricour, J., Tardieu, B., 2005. Port-Miou and Besouan Freshwater Submarine Springs (Cassis-France) Investigations and Works (1964-1978). Water Resources and Environmental Problems in Karst.

Prieto, C., Destouni, G., 2005. Quantifying hydrological and tidal influences on groundwater discharges into coastal waters. Water Resources Research 41 (12).

Rapaglia, J., 2005. Submarine Groundwater Discharge into Venice Lagoon, Italy. Estuaries 28 (5), 705–713.

Röper, T., Greskowiak, J., Massmann, G., 2013. Detecting small groundwater Discharge Springs Using Handheld Thermal Infrared Imagery. Groundwater.

Roy, D. P., Wulder, M. A., Loveland, T. R., Woodcock, C. E., Allen, R. G., Anderson, M. C., Helder, D., Irons, J. R., Johnson, D. M., Kennedy, R., Scambos, T. A., Schaaf, C. B., Schott, J. R., Sheng, Y., Vermote, E. F., Belward, A. S., Bindschadler, R., Cohen, W. B., Gao, F., Hipple, J. D., Hostert, P., Huntington, J., Justice, C. O., Kilic, A., Kovalskyy, V., Lee, Z. P., Lymburner, L., Masek, J. G., McCorkel, J., Shuai, Y., Trezza, R., Vogelmann, J., Wynne, R. H., Zhu, Z., 2014. Landsat-8: Science and product vision for terrestrial global change research. Remote Sensing of Environment 145, 154–172.

Saad, Z., Kazpard, V., Slim, K., Mroueh, M., 2005. Submarine Fresh Water Isotope Study, Lebanon. Journal of Environmental Hydrology 13.

Sabins, F. F., 2007. Remote sensing: Principles and interpretation, 3rd Edition. Waveland Press, Long Grove and Ill.

Santos, I. R., Burnett, W. C., Chanton, J., Dimova, N., Peterson, R. N., 2009. Land or ocean?: Assessing the driving forces of submarine groundwater discharge at a coastal site in the Gulf of Mexico. Journal of Geophysical Research 114 (C4).

Santos, I. R., Eyre, B. D., Huettel, M., 2012. The driving forces of porewater and groundwater flow in permeable coastal sediments: A review. Estuarine, Coastal and Shelf Science 98, 1–15.

Schubert, M., Scholten, J., Schmidt, A., Comanducci, J. F., Pham, M., Mallast, U., Knoeller, K., 2014. Submarine Groundwater Discharge at a Single Spot Location: Evaluation of Different Detection Approaches. Water 6 (3), 584–601.

Schultz, G. A., 1988. Remote Sensing in Hydrology. Journal of Hydrology 100 (1-3), 239–265.

Schütz, T., Weiler, M., 2011. Quantification of localized groundwater inflow into streams using ground-based infrared thermography. Geophysical Research Letters 38 (3).

Scientific Committee on Oceanic Research-Land-Ocean Interactions in the Coastal Zone, 2004. Submarine groundwater discharge: management implications, measurements and effects. IHP-VI Series on Groundwater (5).

Shaban, A., Khawlie, M., Abdallah, C., Faour, G., 2005. Geologic controls of submarine groundwater discharge: application of remote sensing to north Lebanon. Environmental Geology 47 (4), 512–522.

Slomp, C. P., Cappellen, P. v., 2004. Nutrient inputs to the coastal ocean through submarine groundwater discharge: controls and potential impact. Journal of Hydrology 295 (1-4), 64–86.

Spizzico, M., Tinelli, R., 1986. Hydrogeology of Galese Spring. Mar Piccolo of Taranto (South Italy). Proc. 9th Salt Water Intrusion Meeting, Delft, Water Management Group, Delft University of Technology, Delft.

Stefanon, A., 1972. Capture and Exploitation of Submarine Springs. Oceanology International.

Stevanovic, Z., Milanovic, S., Risitc, V., 2010. Supportive Methods for Assessing Effective Porosity and Regulating Karst Aquifers. Acta Carstologia 39 (2), 313–329.

Stüben, D., Sedwick, P., Colantoni, P., 1996. Geochemistry of submarine warm springs in the limestone cavern of Grotta Azzurra, Capo Palinuro, Italy: evidence for mixing-zone dolomitisation. Chemical Geology 131, 113–125.

Suric, M., Loncaric, R., Loncar, N., 2010. Submerged caves of Croatia: distribution, classification and origin. Environmental Earth Sciences (61), 1473–1480.

Swarzenski, P. W., Burnett, W. C., Greenwood, W. J., Herut, B., Peterson, R. N., Dimova, N., Shalem, Y., Yechieli, Y., Weinstein, Y., 2006. Combined time-series resistivity and geochemical tracer techniques to examine submarine groundwater discharge at Dor Beach, Israel. Geophysical Research Letters 33 (24).

Taniguchi, M., 2002. Tidal effects on submarine groundwater discharge into the ocean. Geophysical Research Letters 29 (12).

Tavitian, C., Tiniakos, L., 1991. Underground Karst Water Circulation in Peloponnesus, Greece. In: Günay, G., Johnson, A. I., Back, W. (Eds.), Karst waters & environmental impacts. International Association of Hydrological Sciences, Wallingford, pp. 491–498.

Torgersen, C. E., Faux, R. N., McIntosh, B. A., Poage, N. J., Norton, D. J., 2001. Airborne thermal remote sensing for water temperature assessment in rivers and streams. Remote Sensing of Environment 76 (3), 386–398.

Tsabaris, C., Scholten, J., Karageorgis, A. P., Comanducci, J. F., Georgopoulos, D., Wee Kwong, L. L., Patiris, D. L., Papathanassiou, E., 2010. Underwater in situ measurements of radionuclides in selected submarine groundwater springs, Mediterranean Sea. Radiation Protection Dosimetry 142 (2-4), 273–281.

Umgiesser, G., Scroccaro, I., Alabiso, G., 2007. Mass exchange mechanisms in the Taranto Sea. Transitional Waters Billetin (2), 59–71.

U.S. Geological Survey, 2005. Documentation for the Shuttle Radar Topography Mission (SRTM) Water Body Data Files.
URL http://dds.cr.usgs.gov/srtm/version2_1/SWBD/SWBD_Documentation/Readme_SRTM_Water_Body_Data.pdf

U.S. Geological Survey, 2013. SLC-off Products: Background.
URL http://landsat.usgs.gov/products_slcoffbackground.php

U.S. Geological Survey, 2014a. EarthExplorer.
URL http://earthexplorer.usgs.gov/

U.S. Geological Survey, 2014b. Landsat 8 (L8) Operational Land Imager (OLI) and Thermal Infrared Sensor (TIRS): Calibration Notices.
URL http://landsat.usgs.gov/calibration_notices.php

U.S. Geological Survey, 2014c. USGS Global Visualization Viewer.
URL http://glovis.usgs.gov/

U.S. Geological Survey, 2014d. Using the USGS Landsat 8 Product.
URL http://landsat.usgs.gov/Landsat8_Using_Product.php

Waele, J. d., 2004. Geomorphologic Evolution of Coastal Karst: The Guld Orosei (Central-east Sardinia, Italy). Acta Carstologia 33 (2), 37–54.

Wloczyk, C., Richter, R., Borg, E., Neubert, W., 2006. Sea and lake surface temperature retrieval from Landsat thermal data in Northern Germany. International Journal of Remote Sensing 27 (12), 2489–2502.

Xu, H., 2006. Modification of normalised difference water index (NDWI) to enhance open water features in remotely sensed imagary. International Journal of Remote Sensing 27 (14), 3025–3033.

Yokoyama, R., Tanba, S., Souma, T., 1995. Sea surface effects on the sea surface temperature estimation by remote sensing. International Journal of Remote Sensing 16 (2), 227–238.

Zhu, Z., 2014a. Fmask -Automated clouds, cloud shadows, and snow masking for Landsat 4, 5, 7, and 8 images.
URL https://code.google.com/p/fmask/

Zhu, Z., 2014b. Fmask Variability probability: personal correspondence.

Zhu, Z., Woodcock, C. E., 2012. Object-based cloud and cloud shadow detection in Landsat imagery. Remote Sensing of Environment 118, 83–94.

Zötl, J., 1974. Karsthydrogeologie. Springer-Verlag, Wien and New York.

Software

ArcGIS 10.0

Citavi 4.4

CorelDRAW X6

Erdas Imagine 2013

Fmask 3.2.1 (Zhu and Woodcock, 2012)

Lyx 2.0

Matlab R2013b

Microsoft Office Professional 2010

Appendix

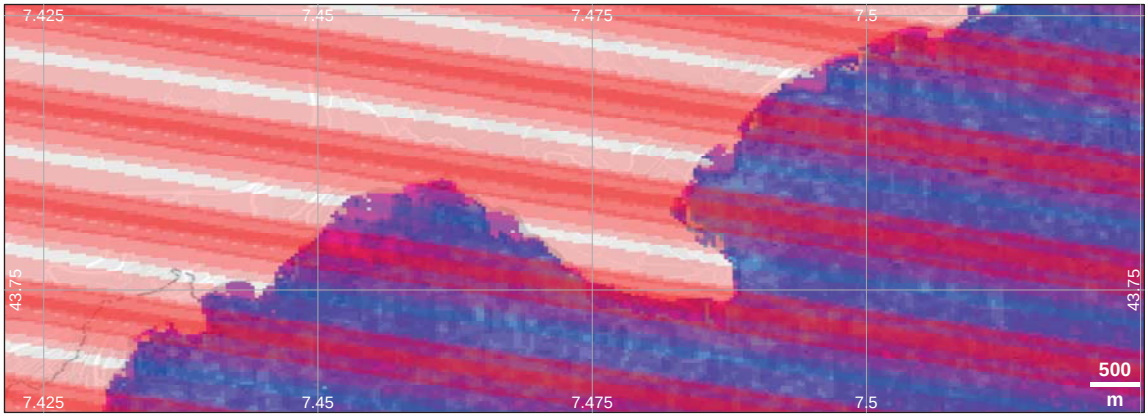

Figure 25: Data gaps (red) which occur through the L7 SLC failure, background shows the range from the L7 low tide dataset.

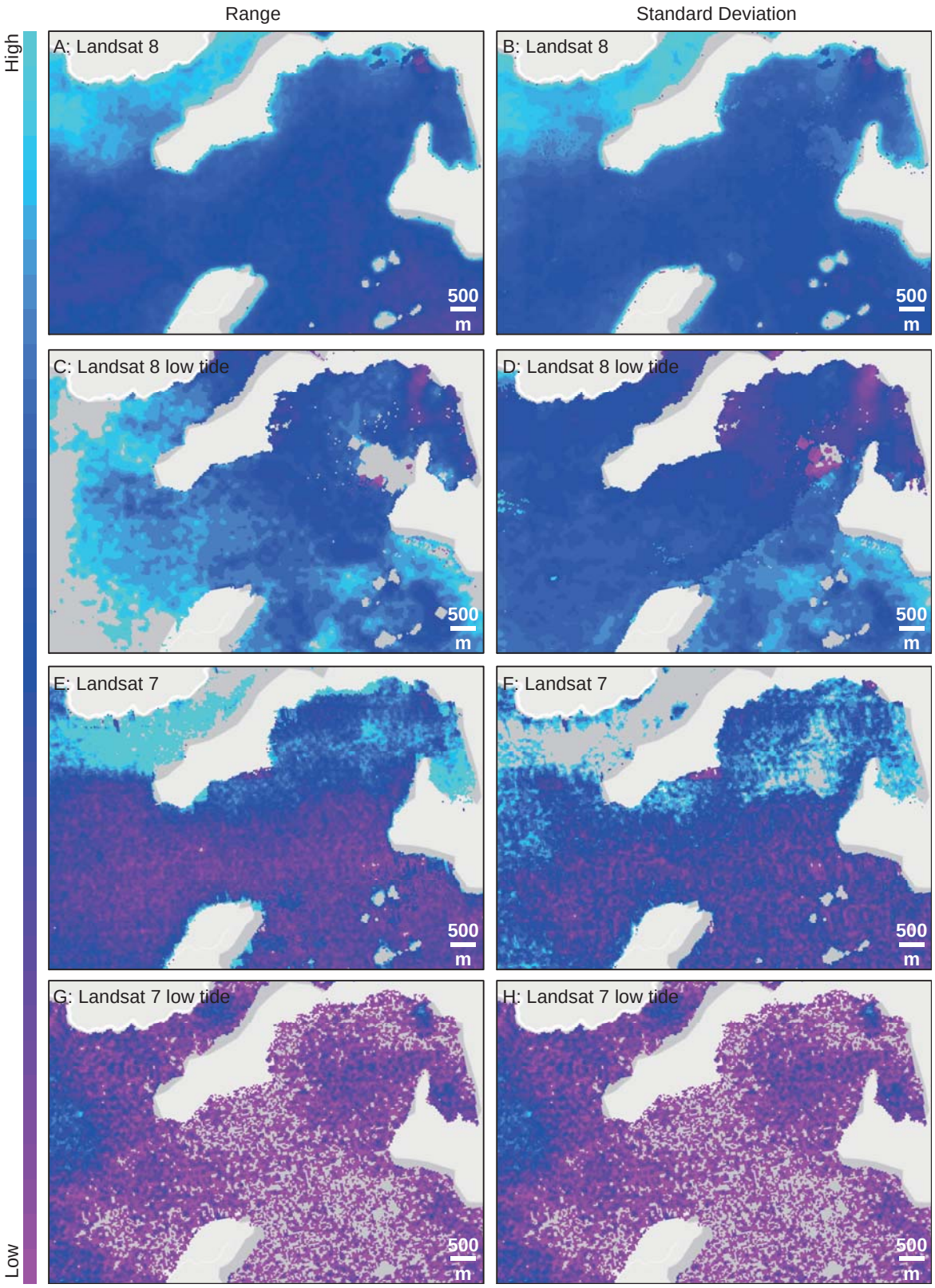

Figure 26: Overview of Range (left column) and standard deviation (right column) for L8 and L7 scenes using either all available thermal scenes or low tide scenes, in the Kas region, Turkey. Note that G and H show the results for two low tide L7 scenes only.

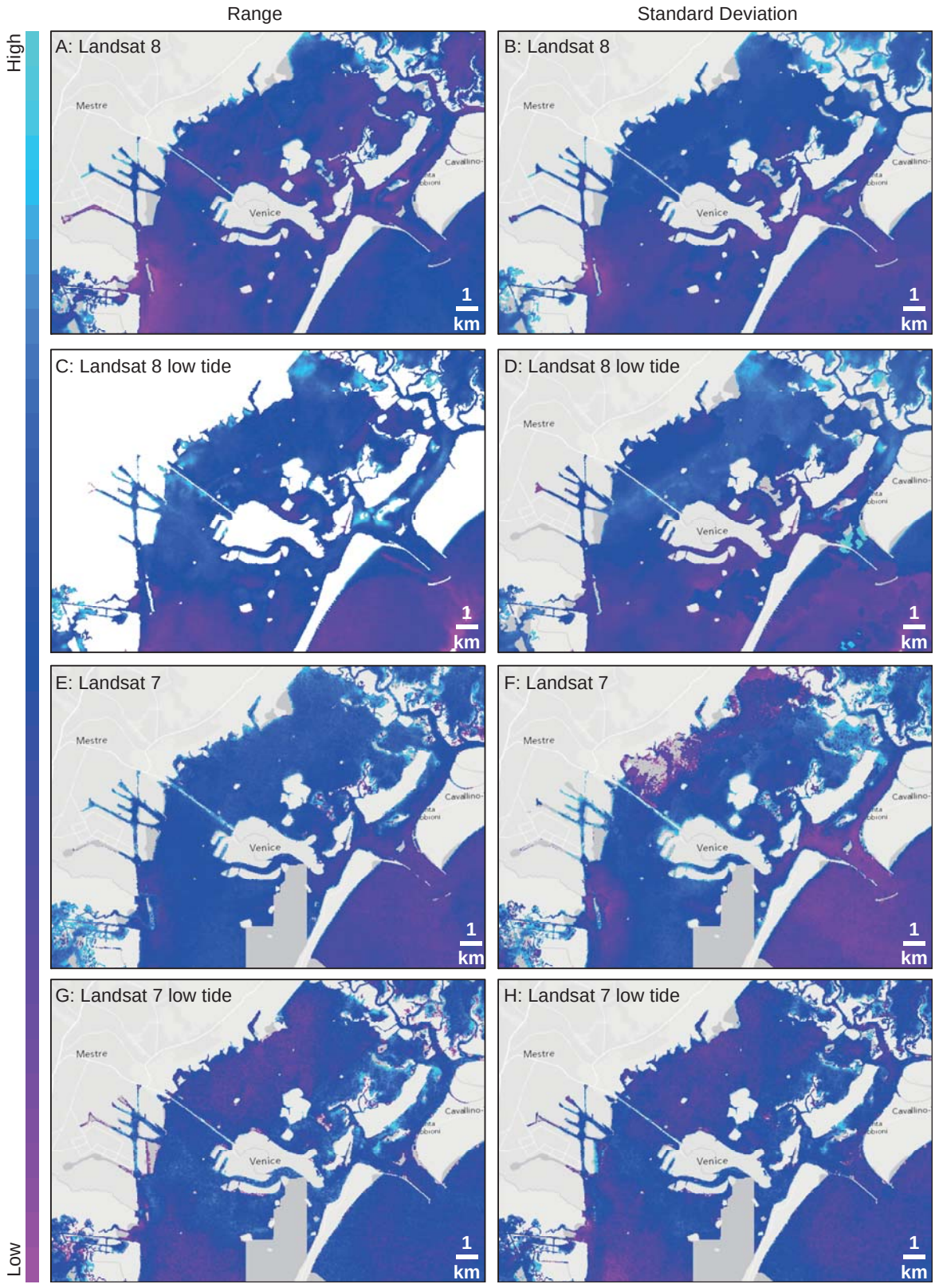

Figure 27: Overview of Range (left column) and standard deviation (right column) for L8 and L7 scenes using either all available thermal scenes or low tide scenes, in the Lagoon of Venice, Italy.

Table 9: Overview of known SGD sites along the Mediterranean coast.

ID	Country	Name	Literature
1	Spain	Moraig-Toix spring	Fleury et al. (2007)
2	Spain	Las Fuentes	Mejías et al. (2012)
3	Spain	Badum	Mejías et al. (2012)
4	Spain	Peniscola	Mejías et al. (2012)
5	Spain	Torre Nova	Mejías et al. (2012)
6	Spain	Alcaufar	Garcia-Solsona et al. (2010)
7	Spain	d'Aigua Dolc	Mandel et al. (1972)
8	Spain	Falconera	
9	France	Port-Miou	Potié et al. (2005)
10	France	Vise (Thau Lagoon)	Fleury et al. (2007)
11	France	Gulf of Lion	Ollivier et al. (2008)
12	France	Cabbé	Gilli (1999b)
13	France	Source du Château	Gilli (1999b)
14	France	Source du Lazaret	Gilli (1999b)
15	France	Source du Palais	Gilli (1999b)
16	France	Source du Cap Ferrat	Gilli (1999b)
17	France	Cap Roux	Gilli (1999b)
18	France	Source de Lisolette	Gilli (1999b)
19	France	Source de Cabuel	Gilli (1999b)
20	France	Sources des Pissarelles	Gilli (1999b)
21	France	Source de la Mata	Gilli (1999b)
22	France	Pompage du Loews & Pompage du Hall du Centenale	Gilli (1999b)
23	France	Pompage du Larvoto	Gilli (1999b)
24	France	Cannes Region	Fleury (2005)
25	Italy/France	Mortola	Fleury et al. (2007)
26	Italy	Grotta Azzurra	Stüben et al. (1996)
27	Italy (Sicily)	Donnalucata	International Atomic Energy Agency (2007)
28	Italy (Sicily)	Ognina	International Atomic Energy Agency (2007)
29	Italy (Sicily)	Cassibile	International Atomic Energy Agency (2007)
30	Italy (Sicily)	Avola	Burnett et al. (2006)
31	Italy (Sicily)	Figarella	Cassinis (1967)
32	Italy (Sicily)	Acqua di Fora	Cassinis (1967)
33	Italy (Sicily)	Praiola	Cassinis (1967)

ID	Country	Name	Literature
34	Italy (Sicily)	Guidaloca	Cassinis (1967)
35	Italy (Sicily)	P. Grottaro	Cassinis (1967)
36	Italy (Sicily)	Cal Bianca	Cassinis (1967)
37	Italy (Sicily)	Cala die Muletti	Cassinis (1967)
38	Italy (Sicily)	Cala Sciaccotta	Cassinis (1967)
39	Italy	Isola la Cura	Rapaglia (2005)
40	Italy	Fusina Terra	Rapaglia (2005)
41	Italy	Citro Galese	Umgiesser et al. (2007)
42	Italy	Citro Le Copre	Umgiesser et al. (2007)
43	Italy	Citro Calandrea	Spizzico and Tinelli (1986)
44	Italy	Citro Mascione	Spizzico and Tinelli (1986)
45	Italy	Citro Citrello	Stefanon (1972)
46	Italy	Aurisina	European Cooperation in the Field of Scientific and Technical Research (2005)
47	Italy (Sardinia)	Bue Marino Cave	Waele (2004)
48	Italy (Sardinia)	Cala Luna Caves	Waele (2004)
49	Italy (Sardinia)	Bel Torrente Cave	Waele (2004)
50	Italy (Sardinia)	Utopia Ispuligidenie	Waele (2004)
51	Croatia	Arbanija	Bonacci et al. (1995)
52	Croatia	Slatina	Bonacci et al. (1995)
53	Croatia	Modric	Suric et al. (2010)
54	Croatia	Zecica	Suric et al. (2010)
55	Croatia	Valun	Kuhta (2004)
56	Croatia	Vrutek	Kuhta (2004)
57	Croatia	Klokun	Matić et al. (2013)
58	Greece	l'Almyros d'Agios Nikolaos	Fleury et al. (2007)
59	Greece	Saronic Gulf	Tavitian and Tiniakos (1991)
60	Greece	Anavalos Kiveri	Fleury et al. (2007)
61	Greece	Chalkida	Tsabaris et al. (2010)
62	Greece	Stoupa	Tsabaris et al. (2010)
63	Greece	Korfos	Tsabaris et al. (2010)
64	Greece	Astros	Food and Agriculture Organization of the United Nations (1964)
65	Greece	Kefallinia	Zötl (1974)

ID	Country	Name	Literature
66	Greece	Areopolis	Marinos et al. (1985)
67	Greece	Pyrgos	Marinos et al. (1985)
68	Greece	Tsairi basin	Prieto and Destouni (2005)
69	Turkey	Patara Evleri	Bayari et al. (2011)
70	Turkey	Komurluk	Bayari et al. (2011)
71	Turkey	Doruk	Bayari et al. (2011)
72	Turkey	Prenses	Bayari et al. (2011)
73	Turkey	Yilan	Bayari et al. (2011)
74	Turkey	Mivini	Bayari et al. (2011)
75	Turkey	Havali	Bayari et al. (2011)
76	Turkey	Cakil	Bayari et al. (2011)
77	Turkey	Likya Batigi	Bayari et al. (2011)
78	Turkey	Altug	Bayari et al. (2011)
79	Turkey	Fakdere	Bayari et al. (2011)
80	Turkey	Fok	Bayari et al. (2011)
81	Turkey	Buza	Bayari et al. (2011)
82	Turkey	Gokkaya	Bayari et al. (2011)
83	Turkey	Ilker Kaptan	Bayari et al. (2011)
84	Turkey	Ovacik springs	Elhatip (2003)
85	Turkey	Gökova Springs	European Cooperation in the Field of Scientific and Technical Research (2005)
86	Syria	BS1 (Bassieh area)	Charideh and Rahman (2007)
87	Syria	BS2	Charideh and Rahman (2007)
88	Syria	BS3	Charideh and Rahman (2007)
89	Syria	BS4	Charideh and Rahman (2007)
90	Syria	BS5	Charideh and Rahman (2007)
91	Syria	BS6	Charideh and Rahman (2007)
92	Syria	BS7	Charideh and Rahman (2007)
93	Syria	TS1 (Tartous Harbour Area)	Charideh and Rahman (2007)
94	Syria	TS2	Charideh and Rahman (2007)
95	Syria	TS3	Charideh and Rahman (2007)
96	Syria	TS4	Charideh and Rahman (2007)
97	Syria	TS5	Charideh and Rahman (2007)
98	Syria	Latakia	Kohout (1966)
99	Lebanon	Boroghlieh M1	Saad et al. (2005)
100	Lebanon	Adloun-Nsarieh M2	Saad et al. (2005)
101	Lebanon	Boroghlieh M3	Saad et al. (2005)
102	Lebanon	Abou Al-Aswad M4	Saad et al. (2005)
103	Lebanon	Adloun M5	Saad et al. (2005)

ID	Country	Name	Literature
104	Lebanon	Adloun M6	Saad et al. (2005)
105	Lebanon	Abou Al-Aswad M7	Saad et al. (2005)
106	Lebanon	Chekka M8	Saad et al. (2005)
107	Lebanon	West Saida M9	Saad et al. (2005)
108	Lebanon	East Saida M10	Saad et al. (2005)
109	Lebanon	Minieh	Shaban et al. (2005)
110	Lebanon	Hai El-Maqateh	Shaban et al. (2005)
111	Lebanon	Bahsa	Shaban et al. (2005)
112	Lebanon	Bahsas-Abu Halqa	Shaban et al. (2005)
113	Lebanon	Fadaous	Shaban et al. (2005)
114	Lebanon	Madfoun-1	Shaban et al. (2005)
115	Lebanon	Madfoun-2	Shaban et al. (2005)
116	Lebanon	Wata El-Borj	Shaban et al. (2005)
117	Lebanon	Helweh-Mar Jerjes-1	Shaban et al. (2005)
118	Lebanon	Helweh-Mar Jerjes-2	Shaban et al. (2005)
119	Lebanon	Helweh-Mar Jerjes-3	Shaban et al. (2005)
120	Lebanon	Tarol-1	Shaban et al. (2005)
121	Lebanon	Tarol-2	Shaban et al. (2005)
122	Lebanon	Halat	Shaban et al. (2005)
123	Lebanon	Bouar-1	Shaban et al. (2005)
124	Lebanon	Bouar-2	Shaban et al. (2005)
125	Lebanon	Tabarja	Shaban et al. (2005)
126	Lebanon	Ma'ameltein-1 El-Borj	Shaban et al. (2005)
127	Lebanon	Ma'ameltein-2 El-Mahatta	Shaban et al. (2005)
128	Lebanon	Ma'ameltein-3 El-Mahatta	Shaban et al. (2005)
129	Lebanon	Jounieh port-1	Shaban et al. (2005)
130	Lebanon	Jounieh port-2	Shaban et al. (2005)
131	Lebanon	Dbayeh	Shaban et al. (2005)
132	Lybia	Ayn Zayanah	European Cooperation in the Field of Scientific and Technical Research (2005)
133	Montnegro	Sopot	Stevanovic et al. (2010)
134	Israel	Dor	Swarzenski et al. (2006)
135	Israel	Nitzanim Area	Prieto and Destouni (2005)
136	Egypt	Marina Lagoon	El-Gamal et al. (2012)

ID	Country	Name	Literature
137	Cyprus	Zakaki Area	Prieto and Destouni (2005)
138	France	Font Estramar	
139	France	La Palme Lagoon	
140	France	Cassis	
141	Israel	Shiqmona	
142	Israel	Akhziv	
143	Spain	Mallorca	
144	Spain	South of Menorca	
145	Spain	Arenys	
146	Spain	Maresme	
147	Spain	Alfacs	
148	Spain	Oliva/Pego	
149	Spain	Gandia,	
150	Spain	Maro	
151	Spain	Aguadulce, Roquetas de Mar	
		Locations known (visual, infrared, salinity)	
153	Croatia	Patan spring	Fleury et al. (2007)
154	Croatia	Blaz spring	Fleury et al. (2007)
155	Marocco	Nador	
156	Tunesia	Gabes	
157	Italy	Lesina	
158	Italy	Oristano	
159	Greece	Almyros	Fleury et al. (2007)
160	Greece (Crete)	Chora Sfakiwn	
161	Greece (Crete)	Bali	
162	Greece (Crete)	Malia	
163	Greece (Crete)	Tsoutsouras	
164	Greece (Crete)	Adiavatos	
165	Malta	St Pauls Bay	
166	Malta	Zurrieq, Blue Grotto	
167	Malta	Marsascata Bay	
168	Malta	Marsaxlokk Bay	

Table 10: Landsat 7 auxiliary data France.

Date	DOY	Scene Center Time	Path	Row	Lat (Center)	Lon (Center)	Atmosph. Profile	Local Atmos-phere	Trans-mission [-]	upwell. Radiance [W/m^2/sr/µm]	downwell. Radiance [W/m^2/sr/µm]	Sun Azimuth [degrees]	Sun Elevation [degrees]	Cloud Cover [%]	T Otsu	T Ele	Low tide
20090805	217	10:07:54	195	30	43.1770	6.35730	Interpolated	summer	0.74	2.01	3.24	136.09	57.18	0	0.26	0.51	
20090906	249	10:07:52	195	30	43.1785	6.35160	Interpolated	summer	0.78	1.65	2.68	146.97	48.65	0	0.27	0.54	
20100520	140	10:09:48	195	30	43.1770	6.36830	Interpolated	summer	0.88	0.77	1.31	137.37	61.26	0	0.26	0.51	
20100621	172	10:09:51	195	30	43.1775	6.37205	Interpolated	summer	0.79	1.45	2.38	131.06	63.43	0	0.23	0.44	
20110811	223	10:11:06	195	30	43.1815	6.36990	Interpolated	summer	0.84	1.20	1.99	139.05	56.31	0	0.27	0.53	x
20110827	239	10:11:04	195	30	43.1760	6.36640	Interpolated	summer	0.85	1.19	1.97	144.48	52.11	0	0.24	0.48	x
20110928	271	10:10:56	195	30	43.1820	6.35130	Interpolated	summer	0.82	1.35	2.24	154.68	41.85	0	0.29	0.56	x
20120712	194	10:12:27	195	30	43.1765	6.39040	Interpolated	summer	0.81	1.43	2.36	132.54	62.00	0	0.21	0.42	
20120728	210	10:12:36	195	30	43.1715	6.40900	Interpolated	summer	0.64	2.91	4.47	135.77	59.39	6	0.22	0.43	
20130512	132	10:13:34	195	30	43.1800	6.35875	Interpolated	summer	0.86	0.98	1.64	140.82	60.19	0	0.23	0.45	x
20130613	164	10:13:22	195	30	43.1800	6.35695	Interpolated	summer	0.69	2.31	3.64	133.48	63.94	0	0.23	0.45	x
20130715	196	10:13:05	195	30	43.1775	6.36995	Interpolated	summer	0.64	2.78	4.33	133.15	61.68	1	0.27	0.53	
20130731	212	10:12:57	195	30	43.1840	6.36235	Interpolated	summer	0.76	1.92	3.10	136.60	58.86	0	0.27	0.53	x
20130816	228	10:12:59	195	30	43.1740	6.40520	Interpolated	summer	0.66	2.58	4.04	141.64	55.19	27	0.22	0.41	x
20130901	244	10:13:11	195	30	43.1740	6.40340	Interpolated	summer	0.68	2.43	3.85	147.22	50.73	14	0.28	0.55	x
20140702	183	10:15:12	195	30	43.1760	6.37375	Interpolated	summer	0.68	2.31	3.66	132.88	63.51	22	0.21	0.40	
20140718	199	10:15:14	195	30	43.1765	6.38835	Interpolated	summer	0.77	1.79	2.90	134.50	61.56	1	0.23	0.45	

Table 11: Landsat 7 auxiliary data Turkey.

Date	DOY	Scene Center Time	Path	Row	Lat (Center)	Lon (Center)	Atmosph. Profile	Local Atmos-phere	Trans-mission [-]	upwell. Radiance [W/m^2/sr/µm]	downwell. Radiance [W/m^2/sr/µm]	Sun Azimuth [degrees]	Sun Elevation [degrees]	Cloud Cover [%]	T Otsu	T Ele	Low tide
19990810	222	08:33:42	179	35	36.0400	28.84000						127.29	60.41	0	0.27	0.52	
20000828	241	08:31:44	179	35	36.0390	28.80500	Interpolated	summer	0.87	1.04	1.72	135.28	55.96	0	0.27	0.53	
20131222	356	08:37:10	179	35	36.0395	28.86800	Interpolated	winter	0.92	0.58	0.97	157.82	27.16	1	0.27	0.50	x
20140123	23	08:37:33	179	35	36.0405	28.78650	Interpolated	winter	0.84	1.11	1.83	152.94	29.79	8	0.26	0.49	x
20140208	39	08:37:40	179	35	36.0380	28.78250	Interpolated	winter	0.83	1.16	1.90	150.24	33.66	12	0.28	0.53	
20140429	119	08:38:01	179	35	36.0395	28.86400	Interpolated	winter	0.78	1.52	2.46	133.59	61.43	23	0.25	0.45	
20140531	151	08:38:11	179	35	36.0365	28.86100	Interpolated	summer	0.70	2.22	3.49	122.00	66.93	3	0.22	0.42	
20140616	167	08:38:12	179	35	36.0390	28.87800	Interpolated	summer	0.71	2.24	3.57	118.09	67.35	0	0.23	0.45	
20140702	183	08:38:18	179	35	36.0405	28.85800	Interpolated	summer	0.76	2.11	3.32	117.50	66.55	0	0.23	0.44	
20140718	199	08:38:20	179	35	36.0375	28.86800	Interpolated	summer	0.57	3.53	5.21	120.47	64.87	1	0.24	0.47	

Table 12: Landsat 7 auxiliary data Italy.

Date	DOY	Scene Center Time	Path	Row	Lat (Center)	Lon (Center)	Atmosph. Profile	Local Atmos-phere	Trans-mission [-]	upwell. Radiance [W/m^2/sr/µm]	downwell. Radiance [W/m^2/sr/µm]	Sun Azimuth [degrees]	Sun Elevation [degrees]	Cloud Cover [%]	T Otsu	T Ele	Low tide
20000620	172	09:50:10	192	28	46.0205	11.95150	Interpolated	summer	0.79	1.59	2.58	136.16	61.81	9	0.28	0.53	
20020930	273	09:46:05	192	28	46.0190	11.94950	Interpolated	summer	0.91	0.61	1.02	155.44	38.33	5	0.32	0.60	
20100328	87	09:50:33	192	28	46.0195	11.96050	Interpolated	winter	0.91	0.51	0.87	149.72	43.03	36	0.33	0.62	x
20100429	119	09:50:33	192	28	46.0240	11.99150	Interpolated	winter	0.81	1.31	2.14	145.92	54.39	39	0.33	0.60	
20100904	247	09:50:38	192	28	46.0245	11.98800	Interpolated	summer	0.73	1.88	2.99	149.74	47.44	39	0.34	0.61	
20110822	234	09:51:45	192	28	46.0240	12.00150	Interpolated	summer	0.61	3.19	4.95	146.08	51.53	0	0.30	0.56	
20111228	362	09:52:20	192	28	46.0240	11.99550	Interpolated	winter	0.92	0.52	0.87	160.46	18.30	2	0.20	0.39	
20120214	45	09:52:29	192	28	46.0225	12.00700	Interpolated	winter	0.93	0.33	0.57	154.24	27.18	20	0.34	0.61	x
20120808	221	09:53:25	192	28	46.0185	12.05150	Interpolated	summer	0.61	3.00	4.66	142.91	55.22	19	0.31	0.59	
20120909	253	09:53:45	192	28	46.0230	12.04000	Interpolated	summer	0.75	1.89	3.09	152.53	45.94	1	0.31	0.59	x
20120925	269	09:53:54	192	28	46.0215	12.04550	Interpolated	summer	0.65	2.50	3.87	156.94	40.47	49	0.33	0.60	
20121230	365	09:54:31	192	28	46.0240	12.00900	Interpolated	winter	0.92	0.47	0.80	160.63	18.51	2	0.30	0.51	
20130216	47	09:54:33	192	28	46.0240	12.00350	Interpolated	winter	0.90	0.55	0.94	154.49	28.25	63	0.32	0.58	
20130304	63	09:54:30	192	28	46.0265	12.00750	Interpolated	winter	0.91	0.56	0.95	152.99	34.04	1	0.32	0.60	x
20130608	159	09:54:03	192	28	46.0240	11.99750	Interpolated	summer	0.73	1.86	3.01	139.59	62.11	18	0.31	0.58	
20130726	207	09:53:39	192	28	46.0250	12.01300	Interpolated	summer	0.58	3.32	5.13	139.78	58.14	11	0.31	0.59	
20130811	223	09:53:35	192	28	46.0180	12.06500	Interpolated	summer	0.71	2.17	3.49	143.75	54.55	13	0.33	0.61	
20131217	351	09:54:40	192	28	46.0215	12.04200	Interpolated	winter	0.95	0.35	0.60	162.29	18.65	23	0.29	0.51	
20140307	66	09:55:09	192	28	46.0205	12.02850	Interpolated	winter	0.87	0.83	1.39	152.96	35.16	0	0.31	0.58	x
20140611	162	09:55:46	192	28	46.0205	12.02250	Interpolated	summer	0.70	2.45	3.94	139.89	62.44	14	0.30	0.57	

Table 13: Landsat 8 auxiliary data France.

Date	DOY	Scene Center Time	Path	Row	Lat (Center)	Lon (Center)	Atmosph. Profile	Local Atmos-phere	Trans-mission [-]	upwell. Radiance [W/m^2/sr/µm]	downwell. Radiance [W/m^2/sr/µm]	Sun Azimuth [degrees]	Sun Elevation [degrees]	Cloud Cover [%]	T Otsu	T Ele	Low tide
20130418	108	10:19:30	195	30	43.1695	6.39135	Interpolated	winter	0.87	1.00	1.68	147.81	54.14	20.23	0.09	0.18	x
20130520	140	10:19:43	195	30	43.1700	6.35810	Interpolated	summer	0.88	0.82	1.39	141.32	62.62	7.37	0.08	0.16	x
20130605	156	10:19:44	195	30	43.1705	6.36175	Interpolated	summer	0.82	1.28	2.13	137.54	64.56	8.86	0.08	0.16	
20130621	172	10:19:36	195	30	43.1695	6.40240	Interpolated	summer	0.78	1.68	2.75	134.97	64.86	2.59	0.07	0.14	x
20130707	188	10:19:41	195	30	43.1690	6.38210	Interpolated	summer	0.73	2.22	3.57	134.77	63.72	6.50	0.10	0.20	x
20130723	204	10:19:39	195	30	43.1695	6.39315	Interpolated	summer	0.71	2.32	3.75	137.13	61.38	0.45	0.09	0.17	x
20130824	236	10:19:44	195	30	43.1685	6.36545	Interpolated	summer	0.60	3.21	4.93	146.70	53.87	10.43	0.09	0.18	
20131011	284	10:19:35	195	30	43.1690	6.36735	Interpolated	summer	0.90	0.69	1.18	160.50	37.93	39.91	0.06	0.12	
20131112	316	10:19:25	195	30	43.1685	6.36365	Interpolated	winter	0.87	0.91	1.53	164.06	27.71	0.30	0.06	0.12	x
20131128	332	10:19:19	195	30	43.1685	6.36365	Interpolated	winter	0.93	0.39	0.68	163.91	24.02	27.15	0.05	0.11	
20131214	348	10:19:15	195	30	43.1685	6.35075	Interpolated	winter	0.90	0.65	1.11	162.69	21.85	6.14	0.05	0.11	
20131230	364	10:19:06	195	30	43.1685	6.35075	Interpolated	winter	0.94	0.41	0.70	160.75	21.48	0.80	0.06	0.11	x
20140115	15	10:18:51	195	30	43.1690	6.37470	Interpolated	winter	0.91	0.60	1.02	158.47	23.00	2.83	0.05	0.11	
20140320	79	10:18:07	195	30	43.1695	6.34520	Interpolated	winter	0.85	1.03	1.72	150.72	42.98	57.24	0.08	0.15	
20140405	95	10:17:52	195	30	43.1695	6.34520	Interpolated	winter	0.82	1.30	2.16	148.91	49.18	4.37	0.08	0.16	
20140507	127	10:17:19	195	30	43.1695	6.34890	Interpolated	summer	0.79	1.49	2.44	143.38	59.52	55.25	0.07	0.14	
20140523	143	10:17:11	195	30	43.1695	6.40420	Interpolated	summer	0.85	1.13	1.89	139.60	62.80	7.53	0.08	0.16	
20140608	159	10:17:22	195	30	43.1690	6.38760	Interpolated	summer	0.82	1.41	2.36	135.95	64.44	2.21	0.05	0.11	

Table 14: Landsat 8 auxiliary data Turkey.

Date	DOY	Scene Center Time	Path	Row	Lat (Center)	Lon (Center)	Atmosph. Profile	Local Atmos-phere	Trans-mission [-]	upwell. Radiance [W/m^2/sr/µm]	downwell. Radiance [W/m^2/sr/µm]	Sun Azimuth [degrees]	Sun Elevation [degrees]	Cloud Cover [%]	T Otsu	T Ele	Low tide
20130520	140	08:42:49	179	35	36.0320	28.84150	Interpolated	summer	0.86	1.17	1.95	127.44	66.66	0.13	0.07	0.14	
20130605	156	08:42:51	179	35	36.0320	28.84650	Interpolated	summer	0.82	1.46	2.41	121.90	68.11	0.84	0.07	0.13	
20130621	172	08:42:43	179	35	36.0330	28.88450	Interpolated	summer	0.77	1.94	3.17	118.84	68.10	0.48	0.08	0.15	
20130707	188	08:42:47	179	35	36.0320	28.86900	Interpolated	summer	0.73	2.38	3.74	119.42	66.98	1.92	0.09	0.16	
20130723	204	08:42:46	179	35	36.0330	28.87700	Interpolated	summer	0.75	2.14	3.47	123.46	65.00	1.10	0.08	0.16	
20130808	220	08:42:49	179	35	36.0320	28.86550	Interpolated	summer	0.81	1.74	2.86	129.89	62.25	0.06	0.07	0.16	
20130925	268	08:42:41	179	35	36.0335	28.87350	Interpolated	summer	0.84	1.35	2.23	151.08	49.39	0.36	0.07	0.15	
20131011	284	08:42:41	179	35	36.0305	28.85700	Interpolated	summer	0.77	1.86	3.04	155.98	44.08	0.10	0.07	0.14	x
20131027	300	08:42:32	179	35	36.0335	28.87500	Interpolated	summer	0.91	0.70	1.19	159.26	38.84	0.20	0.07	0.13	
20131112	316	08:42:32	179	35	36.0305	28.85200	Interpolated	winter	0.85	1.20	1.99	160.89	34.13	1.27	0.06	0.13	x
20131214	348	08:42:21	179	35	36.0310	28.83850	Interpolated	winter	0.95	0.31	0.55	159.93	28.18	1.22	0.05	0.11	
20140115	15	08:41:57	179	35	36.0320	28.86550	Interpolated	winter	0.81	1.33	2.20	155.40	29.02	20.34	0.07	0.13	
20140216	47	08:41:38	179	35	36.0305	28.84850	Interpolated	winter	0.90	0.72	1.23	150.00	36.67	0.67	0.07	0.14	x
20140320	79	08:41:14	179	35	36.0310	28.83700	Interpolated	winter	0.90	0.71	1.21	144.55	48.26	0.72	0.07	0.15	x
20140421	111	08:40:42	179	35	36.0320	28.84400	Interpolated	winter	0.81	1.32	2.21	136.97	59.63	22.23	0.07	0.15	x
20140507	127	08:40:26	179	35	36.0310	28.84400	Interpolated	summer	0.79	1.62	2.64	131.47	63.87	3.05	0.07	0.15	
20140624	175	08:40:31	179	35	36.0330	28.88700	Interpolated	summer	0.89	0.94	1.58	117.83	67.58	0.66	0.07	0.14	
20140710	191	08:40:39	179	35	36.0320	28.87700	Interpolated	summer	0.83	1.55	2.53	119.10	66.32	0.11	0.07	0.14	

Table 15: Landsat 8 auxiliary data Italy.

Date	DOY	Scene Center Time	Path	Row	Lat (Center)	Lon (Center)	Atmosph. Profile	Local Atmos-phere	Trans-mission [-]	upwell. Radiance [W/m^2/sr/µm]	downwell. Radiance [W/m^2/sr/µm]	Sun Azimuth [degrees]	Sun Elevation [degrees]	Cloud Cover [%]	T Otsu	T Ele	Low tide
20130413	103	10:00:09	192	28	46.0155	12.05050	Interpolated	winter	0.83	1.17	1.95	151.52	50.22	14.46	0.11	0.22	
20130515	135	10:00:20	192	28	46.0165	12.01350	Interpolated	summer	0.83	1.18	1.99	146.87	59.68	28.78	0.11	0.21	
20130616	167	10:00:19	192	28	46.0160	12.03100	Interpolated	summer	0.61	3.12	4.86	140.92	63.20	18.03	0.12	0.23	x
20130702	183	10:00:20	192	28	46.0160	12.03150	Interpolated	summer	0.70	2.28	3.67	139.82	62.52	7.82	0.11	0.22	x
20130718	199	10:00:20	192	28	46.0160	12.03700	Interpolated	summer	0.71	2.30	3.71	140.96	60.48	29.75	0.11	0.21	
20130803	215	10:00:22	192	28	46.0160	12.02750	Interpolated	summer	0.75	2.26	3.66	144.08	57.31	0.26	0.10	0.19	
20130819	231	10:00:23	192	28	46.0165	12.01950	Interpolated	summer	0.63	2.83	4.49	148.42	53.21	11.74	0.12	0.23	
20130904	247	10:00:24	192	28	46.0165	12.01000	Interpolated	summer	0.71	2.32	3.70	153.15	48.33	1.60	0.11	0.22	
20131107	311	10:00:06	192	28	46.0165	12.01200	Interpolated	winter	0.84	1.12	1.85	165.12	26.53	6.01	0.09	0.16	
20140331	90	09:58:35	192	28	46.0160	11.99600	Interpolated	winter	0.91	0.58	1.00	152.06	45.07	6.28	0.11	0.22	
20140416	106	09:58:18	192	28	46.0165	12.00000	Interpolated	winter	0.96	0.24	0.43	150.48	51.03	8.75	0.12	0.23	
20140518	138	09:57:53	192	28	46.0160	12.03500	Interpolated	summer	0.75	1.69	2.75	145.32	60.02	49.39	0.12	0.22	
20140603	154	09:57:59	192	28	46.0160	12.03700	Interpolated	summer	0.78	1.57	2.59	142.10	62.32	32.50	0.13	0.25	x
20140619	170	09:58:04	192	28	46.0160	12.04300	Interpolated	summer	0.76	1.74	2.88	139.61	62.94	42.26	0.12	0.22	x

CD contents

Digital version of this thesis (PDF)

Matlab Codes (*.mat, can be opened using any text editor)

Note: Codes are not running since they are related to programs from other authors e.g. Fmask from Zhu and Woodcock (2012).

- A_WaterIndices
- B_Cloudmasking_using_Fmask_by_Zhe
- C_Transect_Long
- D_Threshold_Otsu
- E_Extracting_CloudWater_from_Thermalimages_atmoCorrection
- DEM_inLandsatOrdner